Self-consistent generation of single-plume state for Enceladus using non-Newtonian rheology

A. Rozel[1,2], J. Besserer[3], G. J. Golabek[1], M. Kaplan[4], and P. J. Tackley[1]

[1]Institute of Geophysics, Department of Earth Sciences, ETH Zurich, Zurich, Switzerland, [2]LET Laboratory of Experimental Tectonics, Dipartimento Scienze Geologiche, Università Roma TRE, Roma, Italy, [3]Department of Earth and Planetary Sciences, University of California, Santa Cruz, California, USA, [4]Department of Earth Sciences, University of Southern California, Los Angeles, California, USA

Abstract The thermal dichotomy of Enceladus suggests an asymmetrical structure in its global heat transfer. So far, most of the models proposed that obtained such a distribution have prescribed an a priori asymmetry, i.e., some anomaly in or below the south polar ice shell. We present here the first set of numerical models of convection that yield a stable single-plume state for Enceladus without prescribed mechanical asymmetry. Using the convection code StagYY in a 2-D spherical annulus geometry, we show that a non-Newtonian ice rheology is sufficient to create a localized, single hot plume surrounded by a conductive ice mantle. We obtain a self-sustained state in which a region of small angular extent has a sufficiently low viscosity to allow subcritical to weak convection to occur due to the stress-dependent part of the rheological law. We find that the single-plume state is very unlikely to remain stable if the rheology is Newtonian, confirming what has been found by previous studies. In a second set of numerical simulations, we also investigate the first-order effect of tidal heating on the stability of the single-plume state. Tidal heating reinforces the stability of the single-plume state if it is generated in the plume itself. Lastly, we show that the likelihood of a stable single-plume state does not depend on the thickness of the ice shell.

1. Introduction

Enceladus is one of the most enigmatic satellites of Saturn. Despite the current lack of precise gravitational data (hence, moment of inertia), the estimated structure for the small moon (radius of $\sim$252 km) is a metal-silicate core of radius 150–170 km [*Schubert et al.*, 2007], overlain by a water mantle mostly in the ice state. The icy surface of the small moon exhibits a very large diversity of ages and tectonic features [e.g., *Spencer and Nimmo*, 2013]. In particular, very young terrains are observed at Enceladus's south pole ($<$ 100 Ma) [*Porco et al.*, 2006; *Spencer and Nimmo*, 2013]. This suggests some recent resurfacing event [*Barr*, 2008; *Tobie et al.*, 2008; *O'Neill and Nimmo*, 2010]. This region is currently characterized by a series of jets that feed a plume of vapor and ice particles [*Porco et al.*, 2006; *Spencer et al.*, 2006]. The estimated surface heat flow over Enceladus's south polar terrain (SPT) is 15.8 $\pm$ 3.1 GW [*Howett et al.*, 2011]. If the SPT is approximated by the region of colatitude $\theta \geq 150°$, then the corresponding average heat flux is at least 240 mW m^{-2}.

The observed jets and areas of high heat flux are spatially correlated with long and narrow fractures dubbed the "tiger stripes" [*Spencer et al.*, 2006; *Spitale and Porco*, 2007], and the total power radiating from these structures has recently been estimated to be $\sim$4.7 GW [*Spencer et al.*, 2013]. Although this value represents a significant decrease of the previous lower bound for the SPT thermal emission, it is currently unclear how such a large heat flow can be produced by the tiny moon. A key factor for the anomalous south polar activity is most probably a significant tidal deformation of the ice mantle [*Squyres et al.*, 1983; *Ross and Schubert*, 1989], resulting in deep viscous dissipation [e.g., *Roberts and Nimmo*, 2008a; *Tobie et al.*, 2008; *Běhounková et al.*, 2012], and/or shallow friction [*Nimmo et al.*, 2007] along the tiger stripes. Recently, *Nakajima and Ingersoll* [2012] proposed a model in which liquid water is present under the stripes, leading to vapor condensation and associated heat radiation into space.

Other potential sources of dissipation, such as obliquity-driven tidal dissipation in the ocean [*Tyler*, 2009, 2011; *Chen and Nimmo*, 2011] or subsurface Joule heating [*Hand et al.*, 2011], are probably very small. Note, however, that Joule heating requires the existence of subsurface liquid reservoirs connected to the surface.

In such a case, hot water may directly flow from the bottom of the ice layer to the near surface, which may explain the thermal anomaly and jets associated to the tiger stripes [*Matson et al.*, 2012].

Significant solid tidal dissipation and shallow shear heating both require a strong mobility of the ice mantle, which can only be achieved by the existence of a decoupling liquid layer between the ice mantle and the core. However, *Roberts* [2013] pointed out that even in the absence of such a liquid layer, significant tidal dissipation could be reached inside Enceladus, provided its core is sufficiently disaggregated (i.e., undifferentiated to some degree). The precise location of the thermal anomaly at the south pole only is puzzling. For instance, it might be the result of some diapir-induced reorientation(s) [*Nimmo and Pappalardo*, 2006]. If thermal convection occurs (or has ever occurred) in Enceladus's ice mantle, the associated thermal activity has probably focused below the current anomalous region (SPT). This could be achieved, for instance, by means of a weak (i.e., low viscosity) region in the south polar ice mantle [*Tobie et al.*, 2008; *Han et al.*, 2012] or subsurface [*Roberts and Nimmo*, 2008b], or by thermal convection that focuses above a localized south polar liquid layer [*Besserer et al.*, 2008; *Běhounková et al.*, 2012]. Such a restricted ocean is suggested in particular by the topographic low (0.4–0.8 km) that characterizes the SPT [*Collins and Goodman*, 2007; *Schenk and McKinnon*, 2009; *Walker et al.*, 2012]. A long-term global liquid layer below a convecting ice mantle appears difficult to reconcile with orbital modeling [*Zhang and Nimmo*, 2009], at least during the recent history of the satellite (∼100 Myr). Such a layer would freeze on a typical timescale of ∼30 Myr [*Roberts and Nimmo*, 2008a], unless Enceladus has encountered periods of high eccentricity and melting [*Běhounková et al.*, 2012]. Even the presence of ammonia in the ocean may not prevent it from ultimately freezing [*Roberts and Nimmo*, 2008a; *Mitri and Showman*, 2008]. However, a global ocean might be (or have been) required to account for the formation of current and/or past tiger stripe-like fractures in the south polar region [*Patthoff and Kattenhorn*, 2011].

So far, most of the global models for Enceladus's heat transfer that include a south polar thermal anomaly have obtained this dichotomy by prescribing an a priori asymmetry, namely, a mechanical or heating anomaly in the south polar ice shell near-surface [*Roberts and Nimmo*, 2008b; *Han et al.*, 2012] or at its base [*Běhounková et al.*, 2012, 2013]. One of the few exceptions is the study of *Grott et al.* [2007] that did not prescribe any asymmetry to obtain a convection restricted to one hemisphere. However, these authors found that a very small core (less than ∼100 km in radius), and, consequently, a partially differentiated Enceladus, would be required to obtain a hemispheric convection. This appears difficult to reconcile with the high thermal activity in the south polar regions, and also with the potentially extreme heat fluxes experienced during the satellite's history, as inferred by crater relaxation modeling [e.g., *Bland et al.*, 2012]. A recent model by *Showman et al.* [2013] explains Enceladus's thermal dichotomy by imposing only a topography anomaly at the core's surface. The plausibility of a nonspherical core for Enceladus has, indeed, recently been pointed out by *McKinnon* [2013].

Here, we propose another mechanism for generating a localized single plume with realistic core size and ice mantle parameters. We have run two sets of numerical simulations. In the first set, we map the boundaries of the single-plume state stability field for Newtonian and non-Newtonian rheologies in basally heated cases. In the second set of simulations, we test the first-order impact of tidal heating on the stability of the plume. We do not address the stability of the putative global basal liquid ocean and focus on the conditions for which a single-plume state is stable.

This article only investigates the global thermomechanical state of Enceladus. We focus on the likelihood of the single-plume state. Secondary features such as melting or plasticity which would generate the main topographic signature are not investigated in the present study. Time-dependent mechanisms are sometimes mentioned, but we did not intend to investigate this complexity systematically. For example, we tried only one initial temperature field (see Figure B1). The reader should be aware that in a context of subcritical convection, the initial state can influence the equilibrium state. This study presents a detailed example of thermal subcritical convection in which a classical non-Newtonian rheology can result in a possible convective state for Enceladus, even if tidal heating is nonnegligible.

The remainder of this article is organized as follows: section 2 briefly reviews the rheological mechanisms and thermal convection regimes. The physical problem and the numerical setup used in the present study are detailed in section 3. The results section (4) is then divided in two parts, dealing with convection without and with tidal heating, respectively. The final sections are devoted to the discussion and the conclusions.

2. Rheology and Convection Regimes

2.1. Temperature, Stress, and Grain Size Dependence

The rheology of ice I has been experimentally investigated for several decades [*Duval et al.*, 1983; *Jacka and Maccagnan*, 1984; *Ashby and Duval*, 1985; *Jacka and Jun*, 1994; *Goldsby and Kohlstedt*, 2001]. It is usually assumed that the viscous equilibrium strain rate of ice I under constant shear stress can be described by

$$\dot{\epsilon} = \dot{\epsilon}_{\text{diff}} + \dot{\epsilon}_{\text{GBS}} + \dot{\epsilon}_{\text{disl}}, \tag{1}$$

where $\dot{\epsilon}_i$ are all strain rate tensors, "diff" stands for diffusion creep, "GBS" represents grain boundary sliding basal slip, and "disl" stands for dislocation creep. For each of these deformation mechanisms, the rheological law is considered to follow the form [*Goldsby and Kohlstedt*, 2001; *Hirth and Kohlstedt*, 2003; *Kohlstedt*, 2007]

$$\dot{\epsilon}_i = A \exp\left(-\frac{Q}{RT}\right) \mathcal{R}^{-m} \tau^{n-1} \boldsymbol{\tau}, \tag{2}$$

where A is a constant, Q is an activation enthalpy, R is the gas constant, T is the temperature, $\mathcal{R}$ is the average grain size, m and n are positive, dimensionless experimental constants, usually different for all deformation mechanisms, $\boldsymbol{\tau}$ is the deviatoric part of the stress tensor, and τ is the associated second invariant.

The effect of temperature on the rheology is very important and will be discussed in this section. The average grain size $\mathcal{R}$ is often considered constant in simulations of convection. However, the grain size may vary over orders of magnitude and strongly influence the rheology and the large-scale convection regime of planets and satellites [*Hall and Parmentier*, 2003; *Barr and Pappalardo*, 2005; *Barr and McKinnon*, 2007; *Solomatov and Reese*, 2008; *Rozel*, 2012]. The second invariant of the stress tensor is used in equation (2) to represent the effect of the density of dislocations in the deforming material [*Poirier*, 1985]. The value of the stress exponent n typically lies between 1 and 6, depending on the deformation mechanism [*Goldsby and Kohlstedt*, 2001; *De Bresser et al.*, 2001].

The activation enthalpy is written as $Q = E + PV$, where E is the activation energy, P pressure, and V is the activation volume. The activation energy E may take very different values depending on the considered mechanism and range of temperature. For ice I, E has been reported to be between 40 and 190 kJ mol^{-1} [*Kohlstedt*, 1997; *Goldsby and Kohlstedt*, 2001], but is more generally found to be in the range 40–90 kJ mol^{-1} [*Goldsby and Kohlstedt*, 2001] at temperatures relevant for the shells of convecting icy satellites. The activation volume V is on the order of 10^{-5} m^3 mol^{-1} [*Kirby et al.*, 1987]. This is so low that we consider the effect of pressure on the rheology to be negligible for the case of Enceladus ($E/PV \approx 1000$ at the bottom of the ice shell).

Diffusion creep has been pointed out as a potential important flow mechanism in icy satellites [*McKinnon*, 2006; *Běhounková et al.*, 2013], but has never been observed experimentally in ice, due to the fast grain growth rates. *Goldsby* [2007] argued that it is not yet possible to discriminate between Nabarro-Herring [*Nabarro*, 1948; *Herring*, 1950] and Coble [*Coble*, 1963] diffusive creep mechanism. These mechanisms would lead to grain size exponents of $m = 2$ and $m = 3$, respectively. In diffusion creep, the stress exponent is equal to unity as far as the density of dislocation does not play any significant role in this case. *Goldsby* [2007] argues that the activation energy E should be around 50 kJ mol^{-1} in diffusion creep.

The non-Newtonian grain size sensitive creep (GBS) is the dominant deformation mechanism when stress is sufficiently high and grains recrystallize [*Barr and McKinnon*, 2007; *De Bresser et al.*, 2001]. In this regime, the grain size exponent may vary between $m = 1.4$ and $m = 2.5$ [*Goldsby and Kohlstedt*, 2001]. These authors proposed a grain size exponent $m = 1.4$, a stress exponent of $n = 1.8$, and an activation energy close to $E = 50$ kJ mol^{-1}.

In the dislocation regime, no grain size dependence is expected anymore because the deformation is only accommodated by the motion of dislocations. *Goldsby and Kohlstedt* [2001] showed that a stress exponent $n = 4$ and an activation energy $E = 64$ kJ mol^{-1} are acceptable values. This stress exponent is consistent with experimental values obtained for Earth materials [*Hirth and Kohlstedt*, 2003].

Which one of these mechanisms dominates the others is not easy to estimate a priori for the case of icy satellites as the boundaries between regimes depend on stress, temperature, and grain size. In this study,

we investigate two typical rheological cases, considered as end-members: Newtonian and non-Newtonian (stress-dependent) creep. In Newtonian creep, the viscosity is only temperature-dependent ($n = 1$, $m = 0$); this is equivalent to diffusion creep with a homogeneous grain size. As argued below, the non-Newtonian creep we consider here may represent both dislocation and GBS creep, the latter being associated with dynamic recrystallization.

Indeed, grain growth combined with grain size reduction by dynamic recrystallization leads to the stabilization of the average grain size in deformed materials [*Shimizu*, 1998b; *De La Chapelle et al.*, 1998; *De Bresser et al.*, 2001; *Ricard and Bercovici*, 2009; *Rozel et al.*, 2011]. It has often been observed [*Poirier*, 1985; *De Bresser et al.*, 2001; *Shimizu*, 2008] that the average grain size $\mathcal{R}$ converges to a stress-dependent value following a "piezometric" relationship

$$\mathcal{R} = B\tau^{-p}, \tag{3}$$

where p is a constant close to 1–1.5. The factor B is usually considered to be constant, but it has been proposed that it may slightly depend on temperature [*Duval*, 1981; *Frost and Ashby*, 1982; *Shimizu*, 2008; *Rozel et al.*, 2011]. Dynamic recrystallization has also been observed in shear zones on Earth [*Mancktelow*, 1987; *Vissers et al.*, 1995] and has been investigated in laboratory experiments [*Karato et al.*, 1980; *Van der Wal et al.*, 1993; *Zhang et al.*, 2000; *Jung and Karato*, 2001; *Jung et al.*, 2006].

Using the self-consistent, equilibrium grain size (equation (3)) in the rheological law (equation (2)) leads to a non-Newtonian rheology, even for diffusion creep where the stress exponent n is equal to 1 [*Solomatov*, 2001; *Rainey and Stevenson*, 2005; *Barr and McKinnon*, 2007; *Rozel*, 2012]. Whether the recrystallized grain size can be reached is still debated because the pinning of the average grain size by secondary phases can slow down grain growth [*Durand et al.*, 2006; *Solomatov and Reese*, 2008; *Bercovici and Ricard*, 2012a, 2012b]. Here we do not consider this time-dependent effect as we focus on the final, equilibrium state of the convection pattern.

In GBS or diffusion creep, if the recrystallized grain size is considered stress-dependent, considering that the grain size is fixed at its piezometric value (i.e., equation (3)) leads to the following constitutive equation:

$$\dot{\epsilon} = C \exp\left(-\frac{E}{RT}\right) \tau^{mp+n-1}\tau, \tag{4}$$

where C is a new constant obtained from A and B.

Using the parameters relevant for the case of the ice [*Goldsby and Kohlstedt*, 2001; *Shimizu*, 2008], *Barr and McKinnon* [2007] showed that the equivalent stress exponent of the GBS creep is equal to $n' = mp + n = 1.4 \times 1.25 + 1.8 = 3.55$. In diffusion creep, the equivalent stress exponent would be between 2.5 and 3.75, depending on the grain size exponent. In dislocation creep, the stress exponent is usually considered to be between 3 and 5. In this study, we use both $n' = 1$ for Newtonian creep and $n' = 3.55$ (for sake of consistency with GBS creep obtained by *Barr and McKinnon* [2007]) for non-Newtonian creep.

The viscosity is obtained from the general relation $\tau = 2\eta\dot{\epsilon}$ and the constitutive equation (4). This leads to the usual formulation of a non-Newtonian viscosity

$$\eta(T, \dot{\epsilon}) = \frac{1}{2\,C^{1/n'}} \exp\left(\frac{E}{n'RT}\right) \dot{\epsilon}^{\frac{1-n'}{n'}}, \tag{5}$$

where $\dot{\epsilon}$ is the second invariant of the strain rate tensor. Equation (5) shows that the temperature-dependence of the viscosity critically depends on the equivalent stress exponent n', present in the exponential [*Christensen*, 1983].

In this study we explore a range of activation energies ranging from 3 to 60 kJ mol^{-1}. This is equivalent to a range of stress exponents for a given activation energy. A large stress exponent n' would dramatically diminish the viscosity contrast across the ice mantle [*Christensen*, 1983] and bring Enceladus to a sluggish lid state, even using the value of the activation energy suggested by experiments [*Goldsby and Kohlstedt*, 2001].

Equation (5) contains a highly nonlinear term, $\dot{\epsilon}^{(1-n')/n'}$; its first-order effect can, however, be taken into account using boundary layer theory [*Solomatov*, 1995]. Various authors [*Parmentier et al.*, 1976; *Parmentier and Morgan III*, 1982; *Christensen*, 1983] showed that similar convection patterns can be obtained with and without non-Newtonian rheologies, if one carefully adapts the activation energy and volume and the prefactors of the rheological law. Isoviscous, sluggish, and stagnant lid convection regimes are predicted by

Solomatov [1995] for the non-Newtonian case, while no major difference is expected in convection style compared to a Newtonian rheology. The present study shows that this is not always true as in the case of large aspect ratio (and curvilinear) spatial domains.

2.2. Degree-One, Single-Plume State, and Subcritical Convection

The convective regime of Enceladus, presumed here, is close to a degree-one. The so-called "single-plume state" is defined by a single upwelling surrounded by a quasi-cylindrical downwelling region, itself embedded into a nonconvecting region. The degree-one convection is characterized by a large-scale upwelling in a hemisphere and a broad downwelling in the opposite part of the convecting body [see *Grott et al.*, 2007, for the specific case of Enceladus]. Degree-one convection is then very symmetrical, while single-plume state is not. Yet one may expect that the parameters found important to generate the degree-one state are also required to obtain the single-plume state, seemingly the most similar convection regime. We briefly review these parameters in the present section, together with what may potentially generate an asymmetrical flow.

Degree-one convection is suspected to be responsible for the Martian crustal dichotomy [*Wise et al.*, 1979; *Harder and Christensen*, 1996; *Roberts and Zhong*, 2007; *Keller and Tackley*, 2009; *Šrámek and Zhong*, 2012] and may also have been active in the Earth and the early Moon [*Stevenson*, 1980; *Zhong et al.*, 2000]. *Yoshida and Santosh* [2011] reviewed the possibility of the degree-one and -two convection regimes in the Earth's mantle.

Several parameters have been found to produce a degree-one convection. This convection mode is expected in planets or moons having a relatively small core [*Schubert et al.*, 1990; *Zhong et al.*, 2000; *Grott et al.*, 2007]. Radiogenic heating along with a temperature-dependent or layered rheology also lead to large wavelength flow [*McNamara and Zhong*, 2005; *van Heck and Tackley*, 2008; *Yoshida*, 2008; *Foley and Becker*, 2009]. Finally, and most importantly, a stratified or pressure-dependent rheology produces a low-degree convection pattern [*Weinstein*, 1995; *Tackley*, 1996; *Harder*, 2000; *Zhong and Zuber*, 2001; *Yoshida and Kageyama*, 2006; *Roberts and Zhong*, 2006; *Keller and Tackley*, 2009]. Interestingly, all these characteristics are absent on Enceladus, which seems to have a large core size (compared to its radius), no pressure-dependent rheology, and no radioactive internal heating in its ice shell.

Apart from the degree-one state itself, *Solomatov* [1995] shows that three convection regimes can be reached for different temperature-dependent rheologies and internal Rayleigh numbers: the quasi-isoviscous, sluggish, and stagnant lid regimes. Depending on the convection regime, the flow may be symmetrical or not. The quasi-isoviscous and stagnant lid regimes are symmetrical in their convective region. Upwellings and downwellings have a similar shape (at least in Cartesian geometry) which simplifies the scaling of stresses and temperature distribution using boundary layer theory [*Morris and Canright*, 1984; *Fowler*, 1985; *Solomatov*, 1995; *Reese et al.*, 1998]. In the sluggish regime, the temperature dependence of the viscosity is large enough to produce thick downwellings and too small to decouple what would be a stagnant lid and a convecting region. This situation occurs at a viscosity contrast around 10^2 to 10^4 at low Rayleigh numbers [*Solomatov*, 1995]. From the point of view of temperature distribution, the sluggish state can actually be reached with low viscosity contrast, as predicted by *Solomatov* [1995], or with a largely temperature-dependent viscosity if the pressure dependence is also large [*Christensen*, 1985, 1989]. *Tackley* [1993] and *Yoshida* [2008] have shown that very long wavelength convection occurs in the sluggish lid regime. Thus, the degree-one stagnant lid convective state can be seen as a sluggish state in the convective region, below the lid. Moreover, this sluggish state is more likely reached at low Rayleigh numbers [*Solomatov*, 1995], as in the present study.

Lastly, *Solomatov* [2012] emphasized the stability of single-plumes in subcritical convection conditions [*Segel and Stuart*, 1962; *Busse*, 1967; *Alikina and Tarunin*, 2000]. Two important observations are made in his study. First, it is shown that convection below the critical Rayleigh number can initiate in fluids with a temperature-dependent viscosity if the initial perturbation is sufficiently large (i.e., of finite amplitude). Indeed, the fact that the diffusive state is stable does not mean that a hot convecting case cannot be also stable since the viscosity itself depends on the internal temperature of the domain. Second, *Solomatov* [2012] shows that an isolated subcritical plume can be weak enough to stabilize without generating secondary plumes. This is exactly what we observe in many cases investigated in the present study. We discuss the first-order influence of tidal heating on subcritical convection in section 5.

3. Numerical Setup

We solve the conservation equations in the Boussinesq approximation using the finite difference/finite volume convection code StagYY [*Tackley*, 1993, 2008] in the spherical annulus geometry [*Hernlund and Tackley*, 2008]. The Prandtl number is considered infinite [e.g., *Schubert et al.*, 2001] and the convecting material is incompressible. The equations of conservation of momentum, mass, and energy are, in their nondimensional form [e.g., *Schubert et al.*, 2001]

$$\nabla \cdot \boldsymbol{\tau} - \nabla P = Ra_b T \mathbf{z}, \tag{6}$$

$$\nabla \cdot \mathbf{v} = 0, \tag{7}$$

$$\frac{\partial T}{\partial t} = \nabla^2 T - \mathbf{v} \cdot \nabla T + H_{\text{tide}}, \tag{8}$$

where $\mathbf{v}$ is the velocity of the fluid, Ra_b is the bottom Rayleigh number, $\mathbf{z}$ is a radial, downward-pointing unit vector, and t is time. H_{tide} is an internal heating rate (equation (A1)) and will account for tidal heating in some of our models. Namely, we use a simple scaling based on local viscosity to estimate tidal heating: a maximal heating $H_{\text{tide}} \equiv H$ is reached for an optimal viscosity η_{opt} [*Tobie et al.*, 2003] (cf. section 4.2 and section A1 for details).

The surface temperature is fixed at 73 K and the temperature contrast across the domain is 200 K, consistent with the presence of a layer of liquid water under the ice mantle. Tidal heating is first neglected in section 4.1, and then investigated for a restricted range of parameters in section 4.2.

The thickness of the ice shell is 90 km, a value consistent with the average density of Enceladus [*Schubert et al.*, 2007], and the corresponding inner radius r_i is 162 km. Note that we do not consider here the extreme case of a thin ice shell (< 40 km) that may be required to support shear failure along the tiger stripes [*Olgin et al.*, 2011]. Besides, in our approach, the ocean consists of a thin (~2 km) perennial layer that only acts as a bottom temperature boundary condition. Free-slip boundary conditions are imposed as top and bottom boundaries of the domain. All fields are solved on a grid of 512 × 64 cells with radial mesh refinement at top and bottom boundary layers. A vertical resolution of about 600 m is obtained in the boundary layers with a satisfactory resolution at middepth.

Velocities and pressure are defined on a staggered grid and solved simultaneously using a SIMPLE Revised (SIMPLER)-like method [*Patankar*, 1980] to enforce continuity. Multigrid W cycles and extra coarse-grid relaxations are used to enhance the convergence of the Stokes-continuity equations [*Tackley*, 2008]. The multidimensional positive-definite advection transport algorithm (MPDATA) scheme [*Smolarkiewicz*, 1984] is used to advect the temperature field and a second order finite volume algorithm treats the diffusion part.

To fully investigate the stability of the single-plume state, we chose an asymmetrical initial temperature field (see section B).

This paper is focused on the stability of the single-plume state for various rheological conditions. The question of the evolution in time of the ice shell for different initial conditions is not fully addressed here. We start from an asymmetrical initial temperature field because we are only interested in the likelihood of the equilibrium state for different rheological conditions.

We use a bottom Rayleigh number, as defined by *Solomatov* [1995] for the case of non-Newtonian viscosities:

$$Ra_b = \frac{\alpha \rho g \Delta T h^3}{\kappa \eta_b}, \tag{9}$$

where α is the thermal expansivity, ρ the density, g the gravity acceleration, h the thickness of the ice mantle, κ the thermal diffusivity, and η_b the bottom viscosity at the diffusive strain rate $\dot{\epsilon}_0 = \kappa/h^2$.

The bottom viscosity can be directly obtained from the temperature field when the rheology is Newtonian, but in the case of non-Newtonian rheology, the bottom viscosity is not a priori known because of its strain rate-dependent part (cf. equation (5)). Also, as far as we use a bottom Rayleigh number, our dimensionless
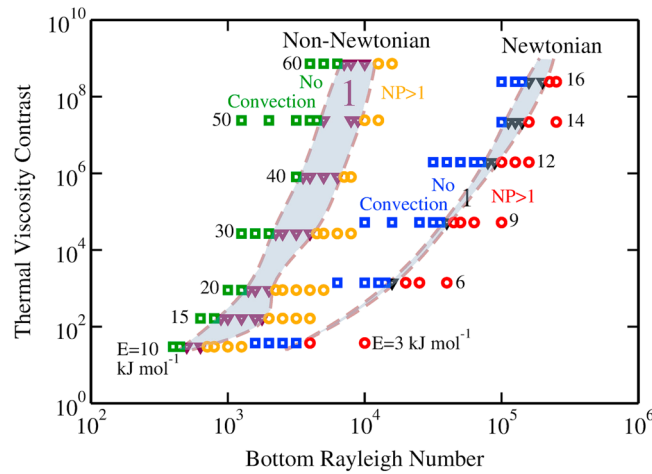
Figure 1. Map of the number of plumes in the $\Delta\eta_T$-Ra_b parameter space (see equations (11) and (9)). Squares: no convection, triangle: single-plume state, and circles: more than one plume. Newtonian (blue, black, and red symbols on the right) and non-Newtonian simulations (green, brown, and orange symbols on the left) are depicted in the same figure for comparison. Number labels correspond to activation energies (in kJ mol^{-1}). "NP" stands for "Number of Plumes." We see that the stability field of the single-plume state (grey area) is located in the neighborhood of the critical Rayleigh number. The single-plume state is more likely to be reached when the rheology is non-Newtonian.

viscosity must be equal to unity for the bottom temperature and a diffusive strain rate. This yields a dimensionless non-Newtonian viscosity η^* given as:

$$\eta^*(T^*, \dot{\epsilon}^*) =$$
$$\exp\left[\frac{E^*}{n'}\left(\frac{1}{T^* + T_0} - \frac{1}{1 + T_0}\right)\right]\dot{\epsilon}^{*\frac{1-n'}{n'}},$$
$$(10)$$

where $E^* = E/(R\Delta T)$, $T^* = T/\Delta T - T_0$, $T_0 = T_S/\Delta T$, and $\dot{\epsilon}^* = \dot{\epsilon}/\dot{\epsilon}_0$. The dimensionless strain rate dependent term $\dot{\epsilon}^{*(1-n')/n'}$ of the viscosity typically converges to values between 10^{-5} and 10^{-1}, thus making the effective bottom Rayleigh number larger than the one initially prescribed in equation (9). Depending on the activation energy, the non-Newtonian viscosity has been found to converge for bottom Rayleigh numbers between 10^2 and 10^5. For numerical stability reasons the maximal dimensionless viscosity is limited to 10^8. The viscosity contrast may reach more than 10 orders of magnitude (cf. Figure 2).

The definition of the viscosity contrast is also problematic in the case of non-Newtonian rheologies, again because of the strain rate-dependent part of the viscosity. We define the "thermal viscosity contrast" (TVC), neglecting the nonlinear part of the viscosity:

$$\Delta\eta_T = \exp\left(\frac{E^*}{n' T_0(1 + T_0)}\right). \qquad (11)$$

For $n' > 1$, the effective viscosity contrast is always greater than the TVC by one or more orders of magnitude. When the rheology is Newtonian, the TVC is the exact viscosity contrast in the simulation because the rheology is only temperature-dependent.

In our non-Newtonian cases, the stress exponent n' is equal to 3.55. Our definition of the thermal viscosity contrast (equation (11)) is valid for all values of the stress exponent. We shall keep in mind that the effective viscosity contrast is slightly higher than the TVC, and that it may reflect the geometry of thermal features, which is hardly predictable a priori.

4. Results

Two sets of simulations have been performed. In the first cases, presented in section 4.1, the domain is heated from below and cooled from above. In the second set (section 4.2), tidal heating is considered as an additional heat source, namely, in order to assess its potential effect on the stability field of the single-plume regime.

4.1. Bottom Heated Simulations
One hundred twenty-three simulations were performed without tidal heating using the spherical annulus geometry. The convective state they reached is summarized in Figure 1. Table 1 reports the number of plumes, Nusselt number, and maximum surface heat flux of each simulation. No periodic or chaotic single-plume state was observed. Hence, Nusselt numbers are only reported for the single-plume simulations reaching a steady state. "Unsuccessful" models developing a higher-order convection pattern were aborted before reaching a steady state. Fifty-four simulations were run using a Newtonian rheology ($n' = 1$), and an exponent $n' = 3.55$ has been used in the other 69 non-Newtonian simulations (cf. Table 1). Since we focus here on the single-plume regime, we did not investigate the number of plumes reached in the simulations developing additional plumes.

Table 1. Results of the Simulations Considering Basal Heating Only[a]

$\text{Log}_{10}\left(Ra_b\right)$	n'	E	N. plumes	Nu	ϕ_{max}
3.5	1	3	no conv.	1	6.67
3.6	1	3	>1	xx	xx
4.15	1	6	no conv.	1	6.67
4.2	1	6	1	1.056	10.90
4.3	1	6	>1	xx	xx
4.55	1	9	no conv.	1	6.67
4.6	1	9	1	1.036	9.18
4.65	1	9	>1	xx	xx
4.85	1	12	no conv.	1	6.67
4.9	1	12	1	1.039	9.10
4.95	1	12	1	1.061	9.99
5.0	1	12	>1	xx	xx
5.0	1	14	no conv.	1	6.67
5.05	1	14	1	1.029	8.61
5.1	1	14	1	1.053	9.60
5.15	1	14	1	1.071	10.21
5.2	1	14	>1	xx	xx
5.15	1	16	no conv.	1	6.67
5.2	1	16	1	1.030	8.61
5.3	1	16	1	1.067	10.03
5.35	1	16	>1	xx	xx
2.65	3.55	10	no conv.	1	6.67
2.7	3.55	10	1	1.218	21.94
2.8	3.55	10	1	1.391	31.57
2.85	3.55	10	>1	xx	xx
2.9	3.55	15	no conv.	1	6.67
2.95	3.55	15	1	1.127	12.34
3.0	3.55	15	1	1.198	14.47
3.1	3.55	15	1	1.373	24.90
3.2	3.55	15	1	1.558	38.41
3.25	3.55	15	1	1.649	44.54
3.3	3.55	15	>1	xx	xx
3.1	3.55	20	no conv.	1	6.67
3.15	3.55	20	1	1.134	11.27
3.2	3.55	20	1	1.169	11.61
3.3	3.55	20	1	1.250	12.65
3.35	3.55	20	>1	xx	xx
3.3	3.55	30	no conv.	1	6.67
3.35	3.55	30	1	1.077	9.92
3.4	3.55	30	1	1.107	10.34
3.5	3.55	30	1	1.164	10.90
3.6	3.55	30	1	1.232	11.67
3.65	3.55	30	>1	xx	xx
3.5	3.55	40	no conv.	1	6.67
3.55	3.55	40	1	1.065	9.36
3.6	3.55	40	1	1.089	9.73
3.7	3.55	40	1	1.140	10.30
3.8	3.55	40	1	1.200	11.02
3.85	3.55	40	>1	xx	xx
3.65	3.55	50	no conv.	1	6.67
3.7	3.55	50	1	1.056	8.99
3.9	3.55	50	1	1.135	10.02
3.95	3.55	50	1	1.164	10.39
4.0	3.55	50	>1	xx	xx
3.8	3.55	60	no conv.	1	6.67
3.85	3.55	60	1	1.040	8.46
3.9	3.55	60	1	1.059	8.85
4.0	3.55	60	1	1.098	9.40
4.1	3.55	60	>1	xx	xx

[a]The activation energies E are expressed in kJ mol^{-1} and the maximum (i.e., above the plume) heat flux ϕ_{max} is in mW m^{-2}. We do not report the Nusselt number for the simulations with a degree greater than one because they have been aborted before reaching their equilibrium state. We report only the single-plume states and the boundaries with the other regimes.

In the Newtonian and non-Newtonian cases, we investigated the stability of the single-plume state for a range of activation energies. For $n' = 1$, we tested values ranging from E from 3 to 16 kJ mol^{-1} and for $n' = 3.55$, we varied E from 10 to 60 kJ mol^{-1}. Figure 1 shows that these two ranges are equivalent in terms of thermal viscosity contrast. The effective viscosity contrast is larger in the non-Newtonian cases.

Figure 1 shows the number of plumes obtained in all cases. The simulations in which the convection naturally ceased (i.e., conductive solutions) are represented by square symbols (blue for $n' = 1$ and green for $n' = 3.55$). The simulations developing the single-plume state are represented by dark triangles (black for $n' = 1$ and brown for $n' = 3.55$) and the circles depict the cases in which several plumes appear (red for $n' = 1$ and orange for $n' = 3.55$). We observe that the single-plume state is always located around the critical Rayleigh number, which tends to indicate that the convection is subcritical. In the Newtonian case, the single-plume state is found in a very small window of Rayleigh numbers for each activation energy. In this case, the presumed regime of Enceladus is easier to reach for the highest activation energies tested. On the other hand, in the non-Newtonian case, the single-plume state is found for a wider range of activation energies and is observed for the more standard experimental value for ice of $E = 50$ kJ mol^{-1} [*Goldsby and Kohlstedt*, 2001]. This study clearly shows that the single-plume state is more likely to be reached using non-Newtonian rheology. Studying Figure 1 might give the impression that single-plume state is found for different effective Rayleigh numbers for Newtonian and non-Newtonian situations. This is not the case as the strain rate-dependency of the viscosity results in an effective Rayleigh number larger than the bottom Rayleigh number (cf. equation (10)).

Figure 2 shows the temperature and viscosity fields for selected simulations. We present two non-Newtonian situations: first (top row) with a large viscosity contrast ($E = 50$ kJ mol^{-1} and $Ra_b = 8.91 \cdot 10^3$) and the other (second row) in the sluggish state ($E = 15$ kJ mol^{-1} and $Ra_b = 1.78 \cdot 10^3$). Such a low activation energy is a way of obtaining a mobile lid convection regime for Enceladus without requiring yielding in the ice shell. The third row shows
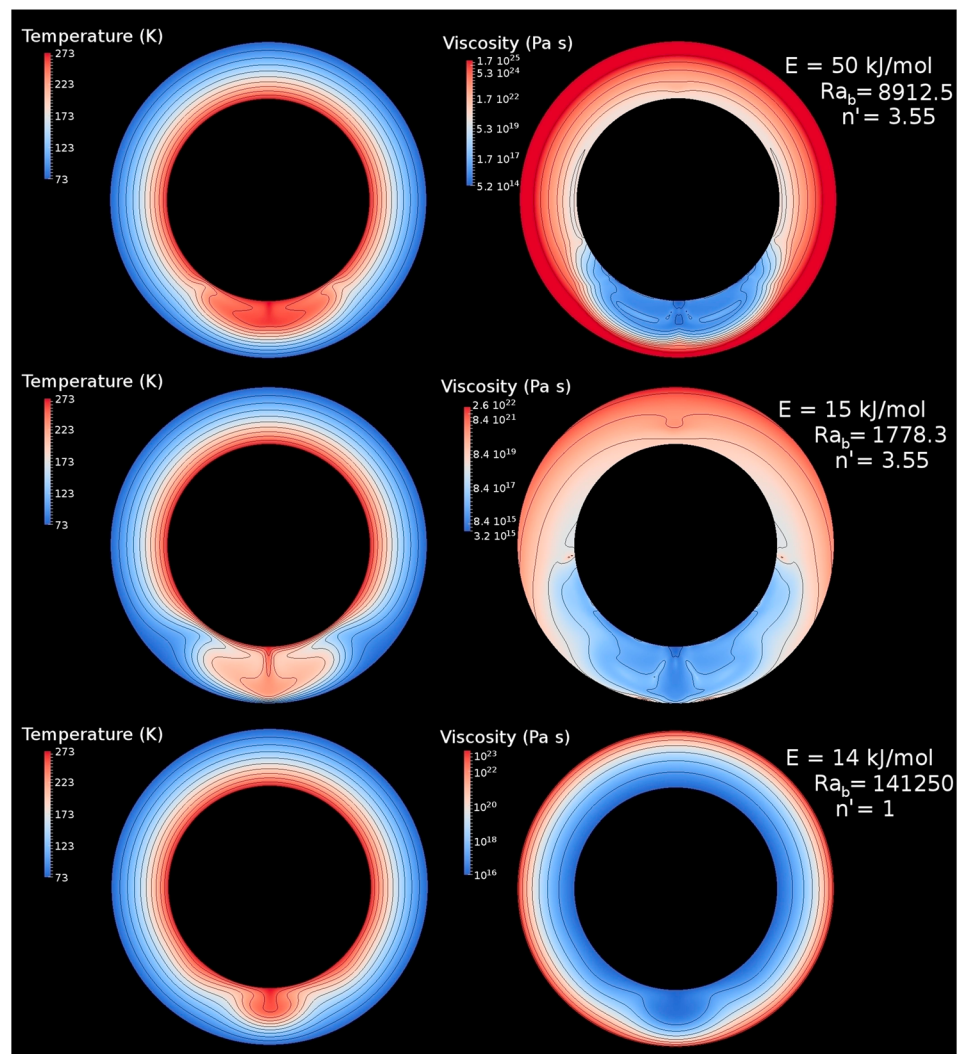
Figure 2. Temperature and viscosity fields in three end-member cases. We represent isocontours every 20 K in the temperature field and every order of magnitude for the viscosity. Very different types of plume can be obtained depending on the rheology. When the thermal viscosity contrast is (top and bottom) high (cf. also Figure 1), the plume, even isolated, is in the stagnant lid regime. (center) The sluggish regime, which explains why its heat flux is larger (cf. Figure 3). In the non-Newtonian case (Figure 2, top and center), the diffusive part of the satellite is stabilized by a higher viscosity region. This explains why the single-plume state is more likely for $n' > 1$.

the case of a Newtonian simulation (E=14 kJ mol^{-1} and Ra_b=1.41·10^5) equivalent to the first row in terms of thermal viscosity contrast. Comparing the viscosity fields in Figure 2, it is apparent why the single-plume state is more likely in a non-Newtonian simulation. Indeed, due to the strain rate-dependent part of the viscosity, the nonconvective parts of the satellite are very viscous because the absence of deformation increases the viscosity by several orders of magnitude relative to the viscosity in the convective region.

Figure 3 shows the Nusselt number and the maximum surface heat flux (see equations (12)–(14)) obtained in all simulations considering basal heating as a function of the bottom Rayleigh number (see Table 1 for the numerical values). Newtonian simulations are represented by purple circles (Nusselt number) and green triangles (maximum heat flux). Non-Newtonian simulations are represented by black circles (Nusselt number) and red triangles (maximum heat flux). Simulations are presented in groups of identical activation energy, depicting the surface heat flux increase with increasing Rayleigh number for each value of E. In all cases, the Nusselt number is extremely low (between 1 and 1.65), since the active, convective part is localized. When n'=1, the Nusselt number stays below 1.08, whereas in the non-Newtonian case, the Nusselt number
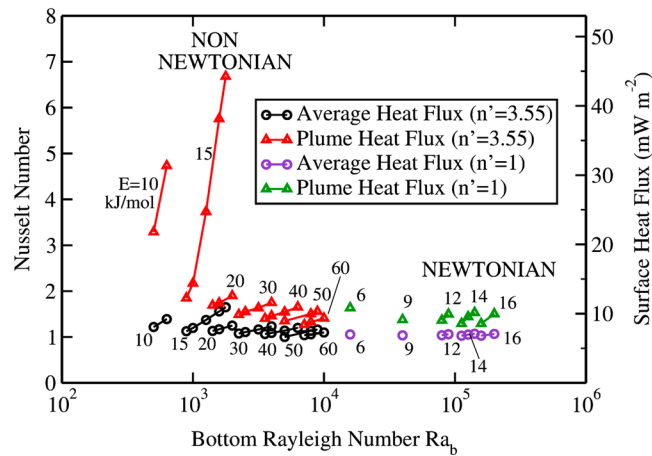
Figure 3. Nusselt numbers and corresponding heat fluxes in the simulations reaching the single-plume state. The circles represent the heat flux averaged over the whole surface (purple: Newtonian and black: non-Newtonian). The triangles represent the maximum heat flux (green: Newtonian and red: non-Newtonian). A large heat flux is observed above the plume in the sluggish regime only in non-Newtonian simulations. The activation energies (kJ mol^{-1}) are detailed in black near the symbols. The dimensional heat fluxes are computed assuming the parameters detailed in Table 2.

reaches 1.65 in the sluggish regime. In the Newtonian cases the maximum heat flux reaches 10.9 mW m^{-2}, while in the non-Newtonian models, it reaches up to 44.54 mW m^{-2}.

The dimensional surface heat flux ϕ can be obtained from the Nusselt numbers using

$$\phi = k\frac{\Delta T}{h}f\,\mathrm{Nu}, \tag{12}$$

where

$$f = (1 + h/r_i)^{-1} \approx 0.64, \tag{13}$$

is the curvature and k is the thermal conductivity (see Table 2 for numerical values). The surface Nusselt number is defined in the top, cold boundary layer using

$$\mathrm{Nu} = -\frac{h}{Sf\Delta T}\int_S \frac{\partial T}{\partial r}\mathrm{d}S, \tag{14}$$

where S is the surface area of Enceladus. The Nusselt number and the surface heat flux are computed considering that the temperature field is axisymmetrical. In the diffusive state, equation (14) ensures that the Nusselt number is equal to one. Presented on the right axis of Figure 3 is also ϕ.

The integrated power over the area above the plume (at the surface in a 60° aperture cone, cf. section 1) corresponds to a thermal output of 0.68 GW, in the non-Newtonian model that reaches flux of 44.54 mW m^{-2}.

Table 2. Physical Parameters Used in This Study

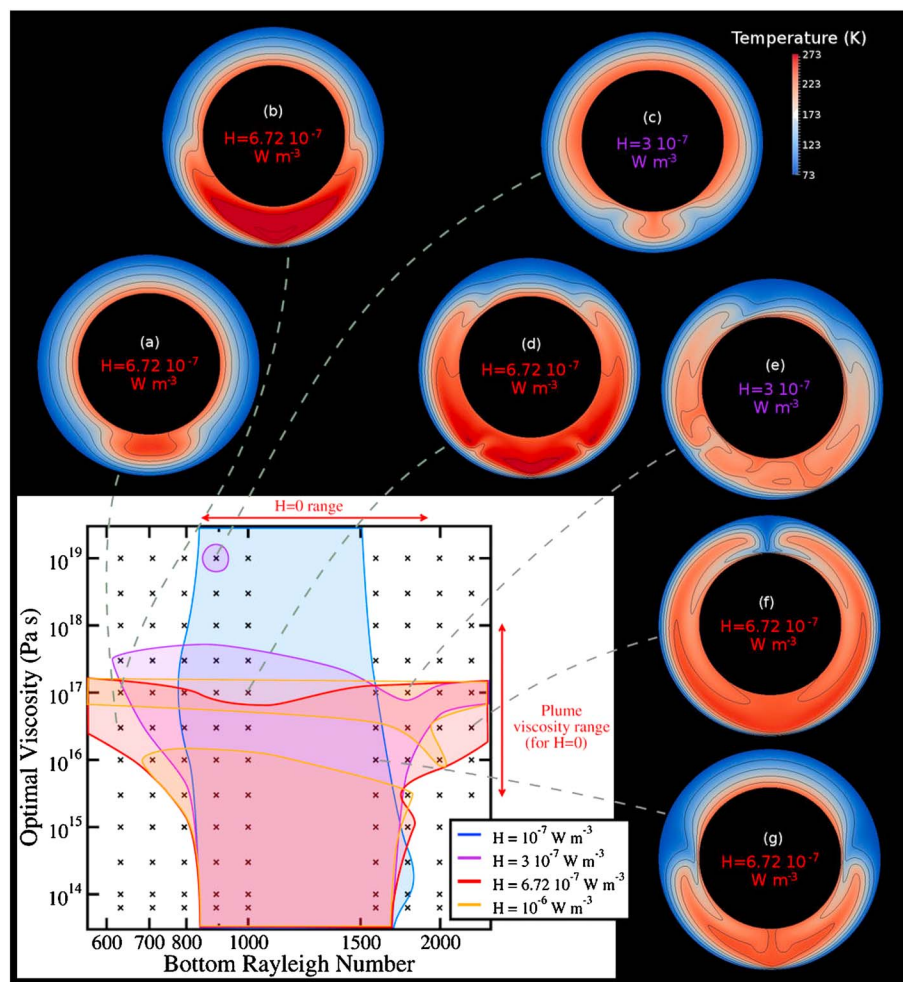| Parameter	Value	Unit	Description
ΔT	200	K	Temperature contrast
T_S	73	K	Surface temperature
r_i	162	km	Inner radius
h	90	km	Ice shell thickness
E	$3 - 60$	kJ/mol	Activation energy
α	$1.5 \cdot 10^{-4}$	1/K	Thermal expansivity
ρ	920	kg/m^3	Density
g	0.112	m/s^2	Gravitational acceleration
κ	$1.5 \cdot 10^{-6}$	m^2/s	Thermal diffusivity
k	3	W/m/K	Thermal conductivity
H	$10^{-7} - 10^{-6}$	W/m^3	Max. tidal heating rate
η_{opt}	$6 \cdot 10^{13} - 10^{19}$	Pa s	Optimal tidal viscosity
Ra_b	$3 \cdot 10^2 - 3 \cdot 10^5$		Bottom Rayleigh number
n	1.8		GBS stress exponent
m	1.4		Grain size exponent
p	1.25		Piezometric exponent
n'	3.55		Effective stress exponent

Figure 4. Map of the single-plume regime found for various bottom Rayleigh numbers, optimal viscosities (η_{opt}), and maximal tidal heating rate H, assuming $E = 15$ kJ/mol and $n' = 3.55$ (from our "best" non-Newtonian, non-tidally heated case). Each "x" symbol represents 4 simulations with different H. Stable single-plume state of various morphologies are found in the shaded regions. The "x" represent the simulations. In the central part of the figure, there is no data, we interpolate the domain boundaries.

This is significantly below the estimated radiated heat flux in the SPT [*Howett et al.*, 2011; *Spencer et al.*, 2013]. However, we show in the following section that tidal heating can help raise the plume heat flux closer to the observed value without destabilizing the single-plume state.

4.2. Bottom and Tidally Heated Simulations

We have shown that the single-plume state is reachable with a comfortable likelihood if the rheology is non-Newtonian. However, it may be argued that tidal heating could bring enough power to generate secondary plumes. Here we investigate the impact of tidal heating on the stability of the single-plume state focusing on the case for which the highest heat flux was obtained in the previous models set ($E = 15$ kJ mol^{-1} and $n' = 3.55$—mobile lid convection, see Figure 2).

Figure 4 depicts the stability field of the single-plume state as determined by 432 additional simulations that reached their stationary or unstationary equilibrium state. Optimal tidal viscosities η_{opt} tested range from $6 \cdot 10^{13}$ to 10^{19} Pa s, in order to take into account our rather poor knowledge of the viscosity relevant to tidal frequencies (see section A). The corresponding maximal heating range is chosen to be $H = 10^{-7} - 10^{-6}$ W m^{-3}, a conservative estimate for Enceladus at its current orbital eccentricity. Bottom Rayleigh numbers' relevant range is defined to be $Ra_b = 600 - 2300$, i.e., around the boundaries found without tidal heating. In this case, Figure 2 shows that the viscosity of the plume typically ranges from 10^{15} to 10^{18} Pa s. Figure 4 shows that tidal heating does modify the boundaries of the stability field of

the single-plume state when the optimal viscosity is in this range. Figure 4 is based on two data blocks (see the two columns of "x" points). The colored curves drawn in between these two blocks are obtained by interpolation.

A low tidal heating power ($H = 10^{-7}$ W m^{-3}) results in a slightly wider stability field that extends to lower Rayleigh numbers: the blue domain deviates to the left around $\eta_{opt} \approx 10^{17}$ Pa s in Figure 4. In contrast, at the highest Rayleigh numbers, secondary plumes nucleate more easily: the stability domain is also shifted to the left. We note that high-optimal viscosities tend to squeeze the stability domain. This is due to the fact that high optimal viscosities result in tidal heating occurring mostly at the edges of the plume or even in the stagnant northern region; this helps the nucleation and growth of secondary plumes.

Using a higher heating power ($H = 3 \cdot 10^{-7}$ W m^{-3}, the purple domain in Figure 4), the stability field of the single-plume state starts to extend to both high and low Rayleigh numbers, when the optimal viscosity is close to the plume viscosity. When the optimal viscosity is greater than $\sim 3 \cdot 10^{17}$ Pa s, tidal heating is sufficient to destabilize the stagnant layer, except in one singular case (case (c) in the example plots of Figure 4, for $Ra_b = 10^3$, $\eta_{opt} = 10^{19}$ Pa s). In this specific example, some heat is generated in the northern, conductive region only, but not enough to generate secondary plumes. This extreme state should hold for higher optimal viscosities (larger than the largest viscosity of the domain), with tidal heating progressively becoming more and more negligible. At the highest Rayleigh numbers, the stability domain of the single-plume state is larger around $\eta_{opt} = 10^{17}$ Pa s, which corresponds exactly to the viscosity of the plume's head (see Figure 2).

The case (e) in Figure 4, using $H = 3 \cdot 10^{-7}$ W m^{-3} and $\eta_{opt} = 10^{17}$ Pa s, is represented even though it is not located in the stability field of the single-plume state. It shows that a cold diffusive block can self-consistently coexist with a convecting and unstationary domain. However, tidal heating is most probably computed too approximately in the broad hot region that is, in addition, not aligned to the south pole (see section A).

At higher tidal heating power, for $H = 6.72 \cdot 10^{-7}$ W m^{-3} (a particularly appropriate value for Enceladus, see section A), optimal viscosities higher than 10^{17} Pa s always result in secondary plumes or convection cessation, depending on Ra_b). We stress here that, interestingly, for η_{opt} between 10^{16} and 10^{17} Pa s, the single-plume state is so stable that it reaches the boundary of our investigation window. The 2-D plots (a), (b), (f), and (g) display the various single-plume morphologies in different locations of the stability domain. The temperature fields of cases (a) and (b), at the same low Rayleigh number, are remarkably different, though these cases are very close in the parameter space. This is due to the fact that the stagnant lid is not broken in case (a), while case (b) presents a "rifting" pattern. It emphasizes the high sensitivity of tidal heating on the chosen optimal viscosity value. Note the locally abnormally high temperature in some cases; this comes from the fact that we do not consider, in our current model, the buffering effect of ice melting (see section 5). These two cases illustrate the potential importance of tidal heating to "break" a stagnant lid and efficiently reshape a convective region if it adds enough power to the plume (no tidal heating is generated in the lid itself). Lastly, a comparison of cases (f), and (g), using the highest Rayleigh numbers, shows that tidal heating can extend the single-plume state to the whole domain, and produce a degree-one convective structure. However, such extreme, broad-plume cases should be considered with caution in our model. Indeed, recall that our approximate method for computing tidal heating does not include latitudinal variations other from those due to the viscosity (see section A). It is well-known that, in the presence of a global decoupling layer (ocean), tidal dissipation in the ice shell is favored in polar regions as compared to equatorial regions [e.g., *Tobie et al.*, 2005]. Case (d) shows a case located outside the single-plume stability field, but potentially a good candidate model for Enceladus [see *Spencer and Nimmo*, 2013, Figure 10]: the northern hemisphere is made of a single diffusive block, the main, broad south polar plume is affected by two small downwellings, but the stagnant lid is only locally broken in one place. However, the latitudinal decrease of tidal heating is probably underestimated in this case, as argued above.

At higher, extreme tidal heating power ($H = 10^{-6}$ W m^{-3}) the single-plume regime's stability domain starts to shrink, as compared to cases with intermediate heating powers. Single-plumes destabilize around $\eta_{opt} = 3 \cdot 10^{16}$ Pa s because tidal heating is so import that degree one convection always tends to form. Note that the latter regime might also be a good candidate for the current state of Enceladus. When the tidal viscosity exactly matches the single-plume's viscosity (i.e., here for $\eta_{opt} = 10^{17}$ Pa s), a large 360° single-plume is able to form. On the contrary, when the optimal viscosity is too low (here $\eta_{opt} = 3 \cdot 10^{16}$ Pa s), a lot of
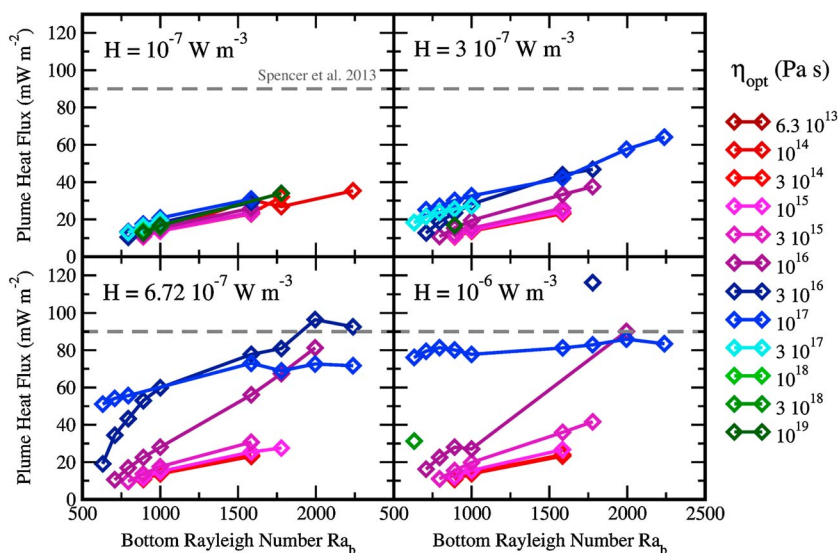
Figure 5. Plume heat flux for all tidally heated cases in the single-plume state. The tidal heating rates are displayed as follows: (top, left) $H = 10^{-7} Wm^{-3}$, (top, right) $H = 3 \cdot 10^{-7} Wm^{-3}$, (bottom, left) $H = 6.72 \cdot 10^{-7} Wm^{-3}$, and (bottom, right) $H = 10^{-6} Wm^{-3}$. Heat fluxes are integrated in a 60° aperture cone and are plotted as a function of the bottom Rayleigh number Ra_b. For each choice of H and η_{opt}, we observe that the heat flux increases with increasing Rayleigh number. The expected value [*Spencer et al.*, 2013] is represented by the grey dashed line (around 90 mW · m^{-2}). Most cases are below 40 mW · m^{-2}. Heat fluxes up to 110 mW · m^{-2} are reported for the extreme cases with the largest tidal heating powers and highest Rayleigh numbers.

energy is produced locally, which tends to widen the head of the plume, but heat production is insufficient to grow the plume up to 360° and secondary plumes have time to establish. These high tidal heating cases should, however, be taken with caution, as we do not include melting in our current model. Such intense tidally induced melting events [e.g., *Roberts and Nimmo*, 2008b; *Běhounková et al.*, 2012] will be taken into account in future models.

As a summary, Figure 5 shows the average heat fluxes obtained above the plume in a 60° aperture cone, for all single-plume cases including tidal heating. The values of these heat fluxes are directly comparable with the measured values rescaled to the same area [i.e., > 90 mW m^{-2}, *Spencer et al.*, 2013]. They are also reported in Table 3. Most of the heat flux values lie between 10 and 40 mW m^{-2}, which corresponds to the $E = 15$ kJ mol^{-1} branch in Figure 3. In these cases, tidal heating then has a negligible effect on the plume. It corresponds to low tidal heating power simulations or large heating power with an "inappropriate" optimal viscosity. In cases above 40 mW m^{-2}, tidal heating is sufficient to develop the plume, which allows more tidal power to be generated, until a stronger, equilibrium single-plume is reached. The corresponding simulations are those which extend the stability domain of the single-plume state in Figure 4.

The average value of the plume heat flux reported by *Spencer et al.* [2013] is also represented by the grey dashed line in Figure 5. Several simulations reach the measured value, usually at the highest values of bottom Rayleigh numbers. Figure 5 shows that the cases with $\eta_{opt} = 10^{16} - 10^{17}$ Pa s and $H > 6 \cdot 10^{-7}$ W m^{-3} reach values close to that reported in *Spencer et al.* [2013]. These cases are, however, far from being realistic as temperatures (hence, tidal heating) are overestimated (no melting). Figure 5 shows that tidal heating can help subcritical-to-weak non-Newtonian convection to reach the measured value of the heat flux of Enceladus without destabilizing the single-plume state. Namely, the effective Rayleigh number is increased.

5. Discussion

The high, localized surface heat flux determined over Enceladus's south polar regions [*Spencer et al.*, 2006; *Howett et al.*, 2011; *Spencer et al.*, 2013] suggests the presence of the sluggish regime obtained here for relatively low activation energies (10–15 kJ mol^{-1}). However, *Goldsby and Kohlstedt* [2001] suggest higher values for E, with which we are still able to obtain the single-plume state but with a smaller surface heat flux (see Tables 1 and 2).

Table 3. Nusselt Numbers, Plume Heat Flux Scaled to a 60° Aperture Cone (mW m^{-2}) and Maximal Flux for the Simulations Including Tidal Heating[a]

$\mathrm{Log}_{10}(Ra_b)$	H	η_{opt}	Nu	ϕ_p	ϕ_{max}	$\mathrm{Log}_{10}(Ra_b)$	H	η_{opt}	Nu	ϕ_p	ϕ_{max}	$\mathrm{Log}_{10}(Ra_b)$	H	η_{opt}	Nu	ϕ_p	ϕ_{max}
2.8	$3\cdot10^{-7}$	$3\cdot10^{17}$	1.249	18.27	28.62	2.95	$6.72\cdot10^{-7}$	$3\cdot10^{15}$	1.042	13.62	25.63	3.2	$1\cdot10^{-7}$	$3\cdot10^{15}$	1.095	23.83	83.04
2.8	$6.72\cdot10^{-7}$	$1\cdot10^{17}$	2.382	51.16	139.88	2.95	$6.72\cdot10^{-7}$	$1\cdot10^{15}$	1.032	11.54	21.53	3.2	$1\cdot10^{-7}$	$1\cdot10^{15}$	1.089	23.25	80.67
2.8	$6.72\cdot10^{-7}$	$3\cdot10^{16}$	1.139	19.10	23.93	2.95	$6.72\cdot10^{-7}$	$3\cdot10^{14}$	1.028	10.90	20.46	3.2	$1\cdot10^{-7}$	$3\cdot10^{14}$	1.087	23.20	80.44
2.8	$1\cdot10^{-6}$	$3\cdot10^{18}$	3.399	31.27	34.71	2.95	$6.72\cdot10^{-7}$	$1\cdot10^{14}$	1.027	10.72	20.14	3.2	$1\cdot10^{-7}$	$1\cdot10^{14}$	1.199	30.48	102.97
2.8	$1\cdot10^{-6}$	$1\cdot10^{17}$	4.699	76.13	228.92	2.95	$6.72\cdot10^{-7}$	$6.3\cdot10^{13}$	1.027	10.71	20.12	3.2	$1\cdot10^{-7}$	$6.3\cdot10^{13}$	1.085	22.94	79.38
2.85	$3\cdot10^{-7}$	$3\cdot10^{17}$	1.356	21.54	33.57	2.95	$1\cdot10^{-6}$	$1\cdot10^{17}$	5.335	80.13	236.35	3.2	$3\cdot10^{-7}$	$1\cdot10^{17}$	1.647	42.17	131.53
2.85	$3\cdot10^{-7}$	$1\cdot10^{17}$	1.240	25.19	49.01	2.95	$1\cdot10^{-6}$	$1\cdot10^{16}$	1.226	28.02	68.12	3.2	$3\cdot10^{-7}$	$3\cdot10^{16}$	1.555	43.97	138.21
2.85	$3\cdot10^{-7}$	$3\cdot10^{16}$	1.050	12.73	22.85	2.95	$1\cdot10^{-6}$	$3\cdot10^{15}$	1.052	15.46	29.73	3.2	$3\cdot10^{-7}$	$1\cdot10^{16}$	1.213	33.35	114.89
2.85	$6.72\cdot10^{-7}$	$1\cdot10^{17}$	2.591	54.18	146.65	2.95	$1\cdot10^{-6}$	$1\cdot10^{15}$	1.034	12.03	22.41	3.2	$3\cdot10^{-7}$	$3\cdot10^{15}$	1.116	25.97	91.55
2.85	$6.72\cdot10^{-7}$	$3\cdot10^{16}$	1.372	34.44	84.98	2.95	$1\cdot10^{-6}$	$3\cdot10^{14}$	1.028	11.18	20.86	3.2	$3\cdot10^{-7}$	$1\cdot10^{15}$	1.096	24.09	84.10
2.85	$6.72\cdot10^{-7}$	$1\cdot10^{16}$	1.033	10.54	19.95	2.95	$1\cdot10^{-6}$	$1\cdot10^{14}$	1.027	10.81	20.28	3.2	$3\cdot10^{-7}$	$3\cdot10^{14}$	1.088	23.23	80.58
2.85	$1\cdot10^{-6}$	$1\cdot10^{17}$	5.030	79.45	229.26	2.95	$1\cdot10^{-6}$	$6.3\cdot10^{13}$	1.027	10.71	20.13	3.2	$3\cdot10^{-7}$	$1\cdot10^{14}$	1.087	23.20	80.43
2.85	$1\cdot10^{-6}$	$1\cdot10^{16}$	1.085	16.21	28.15	3.0	$1\cdot10^{-7}$	$1\cdot10^{19}$	1.326	16.72	33.86	3.2	$3\cdot10^{-7}$	$6.3\cdot10^{13}$	1.086	23.08	79.94
2.9	$1\cdot10^{-7}$	$3\cdot10^{17}$	1.069	12.91	21.34	3.0	$1\cdot10^{-7}$	$3\cdot10^{18}$	1.275	16.03	31.68	3.2	$6.72\cdot10^{-7}$	$1\cdot10^{17}$	4.534	73.00	154.09
2.9	$1\cdot10^{-7}$	$1\cdot10^{17}$	1.054	13.46	23.02	3.0	$1\cdot10^{-7}$	$1\cdot10^{18}$	1.191	16.79	33.00	3.2	$6.72\cdot10^{-7}$	$3\cdot10^{16}$	4.631	77.77	181.93
2.9	$1\cdot10^{-7}$	$3\cdot10^{16}$	1.029	10.40	19.48	3.0	$1\cdot10^{-7}$	$3\cdot10^{17}$	1.122	19.48	40.32	3.2	$6.72\cdot10^{-7}$	$1\cdot10^{16}$	2.420	56.08	173.20
2.9	$3\cdot10^{-7}$	$3\cdot10^{17}$	1.444	23.76	39.05	3.0	$1\cdot10^{-7}$	$1\cdot10^{17}$	1.094	20.78	45.63	3.2	$6.72\cdot10^{-7}$	$3\cdot10^{15}$	1.171	30.69	108.60
2.9	$3\cdot10^{-7}$	$1\cdot10^{17}$	1.306	27.01	52.61	3.0	$1\cdot10^{-7}$	$3\cdot10^{16}$	1.060	18.20	40.45	3.2	$6.72\cdot10^{-7}$	$1\cdot10^{15}$	1.109	25.45	89.53
2.9	$3\cdot10^{-7}$	$3\cdot10^{16}$	1.094	18.71	32.17	3.0	$1\cdot10^{-7}$	$1\cdot10^{16}$	1.042	15.43	32.19	3.2	$6.72\cdot10^{-7}$	$3\cdot10^{14}$	1.092	23.81	82.95
2.9	$3\cdot10^{-7}$	$1\cdot10^{16}$	1.032	10.84	20.29	3.0	$1\cdot10^{-7}$	$3\cdot10^{15}$	1.037	14.23	28.67	3.2	$6.72\cdot10^{-7}$	$1\cdot10^{14}$	1.088	23.29	80.81
2.9	$6.72\cdot10^{-7}$	$1\cdot10^{17}$	2.792	55.63	153.30	3.0	$1\cdot10^{-7}$	$1\cdot10^{15}$	1.036	13.76	27.39	3.2	$6.72\cdot10^{-7}$	$6.3\cdot10^{13}$	1.087	23.05	79.82
2.9	$6.72\cdot10^{-7}$	$3\cdot10^{16}$	1.739	43.25	103.06	3.0	$1\cdot10^{-7}$	$3\cdot10^{14}$	1.035	13.71	27.23	3.2	$1\cdot10^{-6}$	$1\cdot10^{17}$	5.543	81.24	217.69
2.9	$6.72\cdot10^{-7}$	$1\cdot10^{16}$	1.073	16.93	30.40	3.0	$1\cdot10^{-7}$	$1\cdot10^{14}$	1.035	13.69	27.18	3.2	$1\cdot10^{-6}$	$3\cdot10^{16}$	1.253	35.96	125.95
2.9	$6.72\cdot10^{-7}$	$3\cdot10^{15}$	1.024	9.63	18.22	3.0	$1\cdot10^{-7}$	$6.3\cdot10^{13}$	1.035	13.69	27.18	3.2	$1\cdot10^{-6}$	$1\cdot10^{15}$	1.122	26.70	94.40
2.9	$1\cdot10^{-6}$	$1\cdot10^{17}$	5.369	81.39	238.46	3.0	$3\cdot10^{-7}$	$3\cdot10^{17}$	1.628	27.10	54.94	3.2	$1\cdot10^{-6}$	$3\cdot10^{14}$	1.095	24.04	83.89
2.9	$1\cdot10^{-6}$	$1\cdot10^{16}$	1.144	22.49	42.17	3.0	$3\cdot10^{-7}$	$1\cdot10^{17}$	1.439	32.65	83.41	3.2	$1\cdot10^{-6}$	$1\cdot10^{14}$	1.088	23.32	80.95
2.9	$1\cdot10^{-6}$	$3\cdot10^{15}$	1.032	11.01	20.53	3.0	$3\cdot10^{-7}$	$3\cdot10^{16}$	1.191	28.20	71.79	3.2	$1\cdot10^{-6}$	$6.3\cdot10^{13}$	1.088	23.23	80.58
2.95	$1\cdot10^{-7}$	$1\cdot10^{19}$	1.290	12.80	22.44	3.0	$3\cdot10^{-7}$	$1\cdot10^{16}$	1.068	19.46	45.74	3.25	$1\cdot10^{-7}$	$1\cdot10^{19}$	1.459	33.97	117.35
2.95	$1\cdot10^{-7}$	$3\cdot10^{18}$	1.209	12.79	22.29	3.0	$3\cdot10^{-7}$	$3\cdot10^{15}$	1.043	15.32	31.95	3.25	$1\cdot10^{-7}$	$3\cdot10^{14}$	1.212	32.10	109.11
2.95	$1\cdot10^{-7}$	$1\cdot10^{18}$	1.138	13.71	23.51	3.0	$3\cdot10^{-7}$	$1\cdot10^{15}$	1.037	14.23	28.68	3.25	$1\cdot10^{-7}$	$1\cdot10^{14}$	1.115	26.85	96.17
2.95	$1\cdot10^{-7}$	$3\cdot10^{17}$	1.098	16.37	28.24	3.0	$3\cdot10^{-7}$	$3\cdot10^{14}$	1.036	13.76	27.37	3.25	$3\cdot10^{-7}$	$3\cdot10^{16}$	1.719	46.84	152.39
2.95	$1\cdot10^{-7}$	$1\cdot10^{17}$	1.076	17.49	31.55	3.0	$3\cdot10^{-7}$	$1\cdot10^{14}$	1.035	13.71	27.23	3.25	$3\cdot10^{-7}$	$1\cdot10^{16}$	1.322	37.57	130.43
2.95	$1\cdot10^{-7}$	$3\cdot10^{16}$	1.047	14.36	26.76	3.0	$3\cdot10^{-7}$	$6.3\cdot10^{13}$	1.035	13.70	27.20	3.25	$6.72\cdot10^{-7}$	$1\cdot10^{17}$	4.385	68.94	197.09
2.95	$1\cdot10^{-7}$	$1\cdot10^{16}$	1.034	11.95	22.25	3.0	$6.72\cdot10^{-7}$	$3\cdot10^{16}$	2.936	59.88	127.79	3.25	$6.72\cdot10^{-7}$	$3\cdot10^{16}$	5.027	80.94	204.52
2.95	$1\cdot10^{-7}$	$3\cdot10^{15}$	1.029	11.01	20.64	3.0	$6.72\cdot10^{-7}$	$1\cdot10^{16}$	1.167	28.00	75.72	3.25	$6.72\cdot10^{-7}$	$1\cdot10^{16}$	3.662	67.45	187.59
2.95	$1\cdot10^{-7}$	$1\cdot10^{15}$	1.027	10.80	20.27	3.0	$6.72\cdot10^{-7}$	$3\cdot10^{15}$	1.055	17.54	39.10	3.25	$6.72\cdot10^{-7}$	$1\cdot10^{15}$	1.158	27.54	99.52
2.95	$1\cdot10^{-7}$	$3\cdot10^{14}$	1.027	10.70	20.10	3.0	$6.72\cdot10^{-7}$	$1\cdot10^{15}$	1.040	14.98	30.86	3.25	$1\cdot10^{-6}$	$1\cdot10^{17}$	5.696	82.91	221.40
2.95	$1\cdot10^{-7}$	$1\cdot10^{14}$	1.027	10.69	20.09	3.0	$6.72\cdot10^{-7}$	$3\cdot10^{14}$	1.037	14.03	28.11	3.25	$1\cdot10^{-6}$	$3\cdot10^{16}$	7.703	116.11	258.26
2.95	$1\cdot10^{-7}$	$6.3\cdot10^{13}$	1.027	10.69	20.09	3.0	$6.72\cdot10^{-7}$	$1\cdot10^{14}$	1.036	13.74	27.31	3.25	$1\cdot10^{-6}$	$3\cdot10^{15}$	1.386	41.62	148.00
2.95	$3\cdot10^{-7}$	$1\cdot10^{19}$	1.852	16.81	27.44	3.0	$6.72\cdot10^{-7}$	$6.3\cdot10^{13}$	1.036	13.71	27.25	3.3	$3\cdot10^{-7}$	$1\cdot10^{17}$	2.365	57.60	190.42
2.95	$3\cdot10^{-7}$	$3\cdot10^{17}$	1.533	25.57	46.46	3.0	$1\cdot10^{-6}$	$1\cdot10^{17}$	5.233	77.79	236.06	3.3	$6.72\cdot10^{-7}$	$1\cdot10^{17}$	4.747	72.61	229.03
2.95	$3\cdot10^{-7}$	$1\cdot10^{17}$	1.373	30.14	69.75	3.0	$1\cdot10^{-6}$	$1\cdot10^{16}$	1.247	27.03	63.56	3.3	$6.72\cdot10^{-7}$	$3\cdot10^{16}$	6.434	96.44	128.01
2.95	$3\cdot10^{-7}$	$3\cdot10^{16}$	1.137	23.47	48.57	3.0	$1\cdot10^{-6}$	$3\cdot10^{15}$	1.070	19.78	47.32	3.3	$6.72\cdot10^{-7}$	$1\cdot10^{16}$	5.118	81.27	177.57
2.95	$3\cdot10^{-7}$	$1\cdot10^{16}$	1.051	15.29	29.21	3.0	$1\cdot10^{-6}$	$1\cdot10^{15}$	1.043	15.51	32.56	3.3	$1\cdot10^{-6}$	$1\cdot10^{17}$	5.945	85.94	214.59
2.95	$3\cdot10^{-7}$	$3\cdot10^{15}$	1.033	11.88	22.14	3.0	$1\cdot10^{-6}$	$3\cdot10^{14}$	1.037	14.24	28.69	3.3	$1\cdot10^{-6}$	$1\cdot10^{16}$	5.462	90.10	164.46
2.95	$3\cdot10^{-7}$	$1\cdot10^{15}$	1.029	11.01	20.64	3.0	$1\cdot10^{-6}$	$1\cdot10^{14}$	1.035	13.82	27.45	3.35	$1\cdot10^{-7}$	$1\cdot10^{14}$	1.430	35.32	116.07
2.95	$3\cdot10^{-7}$	$3\cdot10^{14}$	1.027	10.79	20.26	3.0	$1\cdot10^{-6}$	$6.3\cdot10^{13}$	1.036	13.73	27.30	3.35	$3\cdot10^{-7}$	$1\cdot10^{17}$	2.806	64.09	208.87
2.95	$3\cdot10^{-7}$	$1\cdot10^{14}$	1.027	10.70	20.10	3.2	$1\cdot10^{-7}$	$1\cdot10^{17}$	1.197	30.90	102.53	3.35	$6.72\cdot10^{-7}$	$1\cdot10^{17}$	4.767	71.65	243.43
2.95	$3\cdot10^{-7}$	$6.3\cdot10^{13}$	1.027	10.70	20.10	3.2	$1\cdot10^{-7}$	$3\cdot10^{16}$	1.155	29.11	98.96	3.35	$6.72\cdot10^{-7}$	$3\cdot10^{16}$	6.045	92.60	175.80
2.95	$6.72\cdot10^{-7}$	$3\cdot10^{16}$	2.399	52.98	115.10	3.2	$1\cdot10^{-7}$	$1\cdot10^{16}$	1.113	25.98	91.02	3.35	$1\cdot10^{-6}$	$1\cdot10^{17}$	5.905	83.49	269.67
2.95	$6.72\cdot10^{-7}$	$1\cdot10^{16}$	1.114	22.48	48.33												

[a]Note: the extreme cases (e.g., $\phi_{max} \sim 200$ mW m^{-2} are most probably not relevant as ice melting is not taken into account in our current model.

Several mechanisms may explain why the effective viscosity contrast of the ice shell is limited. As discussed in section 2.1 the viscosity contrast across the ice layer is highly dependent on parameter choices. The activation energies estimated in laboratory experiments are always obtained at strain rates far from the conditions of the convecting bodies resulting in large uncertainties. For this reason we have considered here a large range around the experimental values. Moreover, we also emphasize in section 2.1 that the effective stress exponent n' has a strong effect on the temperature-dependence of the rheology. The piezometric grain size has not been systematically investigated experimentally in the case of ice I but has a large impact on the stress exponent. The dynamics of dislocations at the microscopic level are poorly understood and are only approximated by the rheological law presented in equation (2). This makes the robustness of the

exponent n' very uncertain. In summary, the stress exponent n' covers many microscopic mechanisms that may be affected by the extrapolation to lower strain rate conditions.

Plasticity has also been found to reduce significantly the viscosity of cold boundary layers above plumes and generate resurfacing events or even a plate-like behavior [*Moresi and Solomatov*, 1998; *Tackley*, 2000; *Stein et al.*, 2004; *van Heck and Tackley*, 2008; *Foley and Becker*, 2009]. This could also be a good candidate for decreasing of the large viscosity contrast reached when we use the experimental value for the activation energy. Plasticity would probably bring our models of Enceladus from stagnant lid single-plume state to sluggish single-plume state, as suggested by our low-activation energy end-member simulations (see Figure 2) and by the recent model of *Showman et al.* [2013] that does include ice shell plasticity.

The question of the history of the satellite has not been investigated in this study. Our simulations start from a thermal state very close to the single-plume state we present in Figure 2 because we are interested here in the stability of this specific state. A regime modification in time from stagnant lid to sluggish single-plume has been observed in tests. When the rheology is non-Newtonian, other stable states may potentially exist using the same rheological parameters depending on the initial temperature conditions [*Barr and Pappalardo*, 2005]. This is left for future studies.

In the present study, the anomalous, low-viscosity non-Newtonian region that develops in the single-plume regime has been artificially centered on the south polar region (see Figure B1). In fact, this region can potentially form anywhere in the ice shell. One can alternatively imagine a localized anomaly (e.g., radiogenic and topographic) at the surface of Enceladus's core that will ultimately favor the development of the single-plume structure at this precise location [*McKinnon*, 2013; *Showman et al.*, 2013]. This might then promote a true polar wander of Enceladus, leading to a natural, poleward reorientation of the structure [*Nimmo and Pappalardo*, 2006]. However, purely thermal density contrasts, as those obtained here, are much less favorable to reorientation than chemical ones [*Nimmo and Pappalardo*, 2006]; the latter may develop through thermochemical convection in Enceladus's ice shell, though [*Han and Showman*, 2005; *Stegman et al.*, 2009]. A potentially more realistic "reorientation" mechanism would be a simple (slow) migration of the low viscosity region toward the south pole, where tidal heating would be optimally efficient. Such thermal attraction would be roughly similar to the slow migration (cell migration or plume clustering) numerically observed by *Solomatov* [2012]. The proposed south polar, weak single plume in the present study might simply be the remnant of a formerly more vigourous convection in Enceladus's history. Even if this mechanism remains highly speculative and must be quantitatively investigated (especially with respect to timescales) with a more realistic tidal heating model, it might provide an interesting way (among others) of moving the locus of thermal activity during Enceladus's history without reorienting the entire ice shell. Indeed, geological mapping of Enceladus has shown a remarkable structural symmetry about the satellite's rotation axis and the direction toward Saturn [*Crow-Willard and Pappalardo*, 2011; *Spencer and Nimmo*, 2013]; this symmetry seems difficult to reconcile with the true polar wander scenario of *Nimmo and Pappalardo* [2006]. In principle, such activity locus migration might also help explain the formation of some broad, potentially compaction-induced basins on Enceladus's surface [*Besserer et al.*, 2013], though the basins (known to date) are mostly located in the northern hemisphere of Enceladus [*Schenk and McKinnon*, 2009; *Nimmo et al.*, 2011]. The precise location of the current thermal anomaly at the south pole, therefore, remains an open question.

Two important characteristics of the solutions we obtained with our model should be stressed here. First, the anomalous, say, "south polar" region of low viscosity in our model resembles the a priori low viscosity structure supposed by *Tobie et al.* [2008] to infer tidal dissipation rates and show that a bottom liquid layer seems necessary to account for a significant tidal dissipation. We show that such a structure may be considered not so artificial if the possibility of non-Newtonian convection on Enceladus is taken into account. The second key point is that we found that convection naturally localizes itself in a region of small angular extent (20 to 60°—if tidal heating is included, this extent can be broader) without the need of a localized basal liquid layer [e.g., *Běhounková et al.*, 2012]. Note that the latter study is focused on more vigorous convection regimes for Enceladus. The northern region of the ice mantle remains in a conductive state, therefore decreasing the ability of the ice shell to evacuate heat in these regions (but still not preventing the putative ocean to ultimately freeze [*Roberts and Nimmo*, 2008a; *Tobie et al.*, 2008; *Běhounková et al.*, 2012]). This might help explain the thermal state of Enceladus consistent with its recent orbital history. Indeed, *Zhang and Nimmo* [2009] have shown that a globally convecting Enceladus would be too dissipative to be

compatible with its recent orbital evolution (considering a standard, relatively low dissipation factor of Saturn). In addition, in this case, the efficiency of even a weak (and tidally heated), or marginal convection [*Barr and McKinnon*, 2007] would lead to the freezing of the putative basal ocean in a few tens of millions of years [*Roberts and Nimmo*, 2008a]. On the other hand, *Zhang and Nimmo* [2009] found that the most favorable thermal state of Enceladus to the orbital constraints would consist of a conductive ice shell over the ocean. Our model in general favors the latter state in most parts of the ice mantle. A conductive ice shell might also help prevent the ocean from freezing if the anelastic behavior (transient creep) of the dissipative ice shell is taken into account [*Shoji et al.*, 2013].

We observe that the localized, low-viscosity convecting region that we obtain contributes to focus tidal heating [*Tobie et al.*, 2008] and therefore yield a thermal feedback, concentrating the hot upwelling in the south polar region [*Běhounková et al.*, 2010]. This, together with possible tidally-controlled melting of the ice shell [*Roberts and Nimmo*, 2008b; *Běhounková et al.*, 2012], would tend to favor the persistence of a liquid layer below the south polar convecting mantle. As argued above, a major limitation of our current model is the lack of a melting mechanism. Such an additional effect would mainly result in lower plume temperatures in the extreme tidally heated cases (e.g., $H = 10^{-6}$ W m^{-3}) and consequently to lower heat fluxes. Such high tidal heating could, for instance, represent past periods of higher eccentricity in Enceladus's history [*Běhounková et al.*, 2012]. Besides, although some of our mobile lid, tidally heated simulations led to interestingly high heat fluxes in the SPT (see Figure 5), tidal heating is probably overestimated in cases with a broad low-viscosity region as we do not consider intrinsic latitudinal variations in our simple, first-order approach (see section A). A fully consistent calculation of tidal dissipation will be one of the main next steps of our model, also taking into account the non-Newtonian behavior in the tidal heating model [*Han and Showman*, 2011]. The current heat production in Enceladus remains puzzling with regard to the most favorable value of 1.1 GW found for the equilibrium tidal dissipation [*Meyer and Wisdom*, 2007] independently of Enceladus's internal structure or thermal state. It could be explained by a current transient state of intense thermal activity, that may be part of a more complex oscillatory thermal [*Tobie et al.*, 2008; *O'Neill and Nimmo*, 2010; *Showman et al.*, 2013] or thermal-orbital history [*Ojakangas and Stevenson*, 1986; *Meyer and Wisdom*, 2008; *Spencer and Nimmo*, 2013]. The answer may alternatively lie in the potentially stronger equilibrium tidal dissipation of Enceladus that would be enabled by a much more dissipative Saturn, as found by recent astrometric measurements [*Lainey et al.*, 2012].

We did not report the grain size obtained in our model because the piezometric approach leads to unreasonably large values (at least 1 m) in this subcritical, low-stress convection framework. Note, however, that terrestrial ice measurements [e.g., *Jouzel et al.*, 1999] and theoretical models [e.g., *Schmidt and Dahl-Jensen*, 2003] point to grain sizes that could reach tens of centimeters to several (even tens of) meters, respectively. We do not expect the grain size to reach such enormous values because Zener pinning may limit the growth [*Smith*, 1948]. In such a case, nonlinear and especially time-dependent processes may occur, which we did not investigate in this study. One could expect that pinning would tend to produce lower stress exponents because the grain size could become more homogeneous than it would be in its piezometric state. Yet, *Bercovici and Ricard* [2012b] showed that this argument may be oversimplified because deformation can instead localize, which would generate large grain-size contrasts. In the range of small stresses we considered here (characteristic of weak-to-subcritical convection), we would expect the dislocations to dominate the deformation mechanisms, because the piezometric grain size is very large. Dislocation creep is then a priori the most appropriate deformation mechanism for subcritical convection. The reason why the piezometric grain size we predict is so high is detailed in section C. A large grain size may prevent the onset of convection in Enceladus's ice shell [*Barr and Pappalardo*, 2005], even if tidal dissipation is considered [*Han and Showman*, 2011; *Běhounková et al.*, 2013]. However, we stress here that the proposed thermal regime for Enceladus consists more in a residual convection in the ice shell. In such weak (subcritical), low-stress convection, ice grain could certainly reach values higher that the critical one for the onset of convection.

Finally, we considered only a thick (90 km) ice shell in the present model. However, the ice shell may be thinner (< 40 km) in order to support shear failure along the tiger stripes [*Olgin et al.*, 2011]. A thinner ice shell also seems to be supported by recent, preliminary interpretations of Enceladus's gravity field [*Hemingway et al.*, 2013; *Stevenson et al.*, 2013]. We briefly show in section D that our proposed single-plume regime for Enceladus is robust to ice shell thickness.

6. Conclusions

We present the first set of numerical simulations of thermal convection applied to Enceladus that address the stability of a weak, single-plume state without prescribed mechanical asymmetry and for a realistic core size. We show that a non-Newtonian rheology can explain this state at Rayleigh numbers just above critical.

In our simulations, the convection regime of Enceladus stabilizes in a typical singular state: a cold, conductive northern hemisphere and a hot plume at the south pole. This state is more likely to remain stable when the rheology is non-Newtonian (whether it is grain size or dislocation-dependent) because the stress-dependent part of the viscosity stabilizes the cold northern hemisphere and, on the contrary, keeps the southern hemisphere active.

In the basally heated simulations, convective heat fluxes from 10 to 45 mW m^{-2} are reported above the plume, for a large range of activation energies and Rayleigh numbers. However, by means of an approximate computation of tidal heating, some of our simulations were able to reach higher heat fluxes (though still below the estimated observed value) without destabilizing the single-plume state. This shows that the combination of non-Newtonian rheology and tidal heating may well describe the present state of Enceladus and deserves further study. The recent improvement of Enceladus's gravity field [*less et al.*, 2013] brings hope to the present single-plume test model.

Lastly, our model shows that a localized ocean [*Běhounková et al.*, 2012] is not necessarily required to consistently generate a hot, active south polar mantle surrounded by purely conductive regions. If such a convective plume actually characterizes Enceladus's ice shell, tidal heating and induced ice melting might contribute to the stabilization of a liquid ocean below part of the southern hemisphere.

Appendix A: An Approximate Method for Tidal Heating

In order to assess the effect of tidal heating on the obtained single-plume regime for Enceladus, we implemented a simple, first-order method for computing this effect in our geometrical framework (spherical annulus). Indeed, tidal deformation and the associated dissipation is essentially a three-dimensional problem. To date, the only model that self-consistently computes Enceladus's solid-state tidal dissipation in a 3-D spherical framework is the one developed by *Tobie et al.* [2008], subsequently used in the coupled, tidally heated convection simulations of *Běhounková et al.* [2010, 2011, 2012, 2013]. In our 2-D annular model, we use an approximate method based on a simple scaling. Our approach is motivated by two fundamental characteristics of our Enceladus model: (1) the presence of a global ocean at the base of the ice shell and (2) the typical localized low viscosity regions obtained (e.g., Figure 2).

As the ice shell is fully decoupled from the core in our model (~2 km global ocean, see Table 2), the tidal strain rate (its average over an orbital cycle) can first be considered as approximately constant throughout the ice shell; though, latitudinal (and longitudinal) variations should ideally be included in a fully consistent model. Tidal dissipation then mainly depends of the local viscosity. For sake of simplicity, we assume the ice shell behaves as an incompressible, Maxwell viscoelastic body at the orbital frequency. We can then write the viscosity-dependent local (dimensional) tidal heating as follows [*Tobie et al.*, 2003; *Han and Showman*, 2010]:

$$H_{\text{tide}} = 2H \frac{\eta \eta_{\text{opt}}}{\eta^2 + \eta_{\text{opt}}^2}, \tag{A1}$$

where H is the maximum dissipation rate, occurring at an optimal viscosity η_{opt}. The latter is simply equal to the ratio μ/ω_0, with μ the shear modulus of the ice shell, and ω_0 the orbital (angular) frequency. For a typical value $\mu = 3.3$ GPa, this yields $\eta_{\text{opt}} \simeq 6.3 \cdot 10^{13}$ Pa s, and a conservative range for H is $10^{-7} - 10^{-6}$ W m^{-3}. As we are dealing here with the full ice shell of Enceladus, not at a local scale like in the Cartesian study of *Tobie et al.* [2003], the constant tidal strain rate hypothesis is, in our case, even a larger approximation. However, equation (A1) can be used as parameterized formula to mimic the 3-D dissipation patterns. As an illustrative example, Figure A1 shows the tidal heating spatial distribution obtained with the viscosity structure used in *Tobie et al.* [2008]. Indeed, these authors consider a fixed south polar viscosity anomaly with a Gaussian shape, roughly similar to the typical localized low viscosity regions we obtain in the first simulation set (without tidal heating). In this specific case, the best pair of parameters (η_{opt}, H) that enables us to
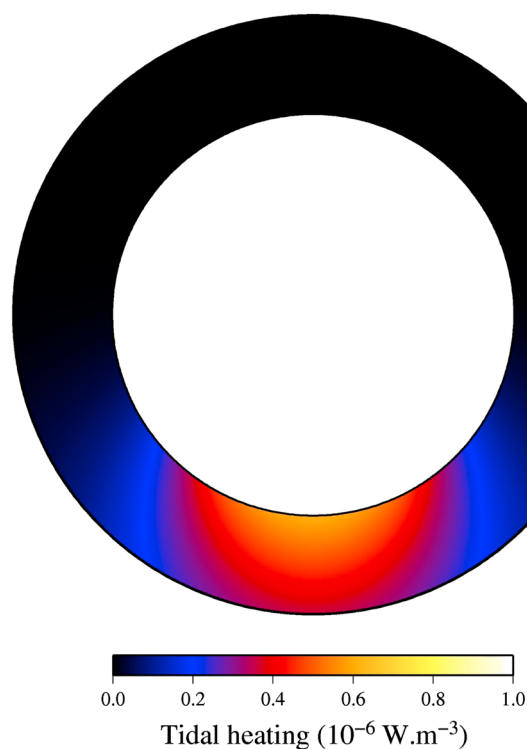
Figure A1. Tidal heating distribution obtained with our approximate method for the Gaussian viscosity anomaly case of *Tobie et al.* [2008]. See Figure 2 for comparison (low-viscosity region with half width of 30°). The global dissipated power, required to be matched, is 3.0 GW. Note that the curvature in this test case is slightly greater from our Enceladus model's curvature: we took here $f = 0.67$ instead of our standard value ($f = 0.64$) in order to match the geometrical setup employed by *Tobie et al.* [2008].

mimic the tidal heating distribution inferred by *Tobie et al.* [2008] was found to be $\eta_{opt} = 6 \cdot 10^{12}$ Pa s and $H = 6.72 \cdot 10^{-7}$ W m^{-3}. The agreement with the distribution obtained by *Tobie et al.* [2008] is remarkable (see their Figure 2), given the simplicity of our method. This is mainly due to the fact that, in this specific case, the low viscosity region is of a limited spatial extent. Therefore, the constant tidal strain rate approximation remains reasonable. Note that a typical vertical cross-section of the full 3-D dissipation field is shown in Figure 2 of *Tobie et al.* [2008], so the above comparison/match is only semiquantitative in nature. Tests with various width of the low-viscosity region, and also with various viscosity contrasts between that region and the remaining ice shell (cf. Figure 1 of *Tobie et al.* [2008]), have shown the approximate method employed in our approach behaves reasonably well for the range of viscosity values considered in this study.

Nevertheless, this approximate method has an important intrinsic limitation that should be kept in mind, in addition to its restriction to Enceladus models with global oceans: the low-viscosity region should be centered on the (here south) polar region. Indeed, for a given viscosity and a global ocean, this location coincides with the locus of the maximal tidal heating. More generally, the simple equation (A1) does not include any intrinsic latitudinal dependence. Therefore, the low-viscosity region cannot have a too broad azimuthal extension. With this respect, cases (d), (e), and (f) of Figure 4 should be considered with caution, and tidal heating and the associated positive thermal feedback are probably overestimated in such cases.

In the present study, in the same spirit as for the range of activation energies considered, we explore a range of values for the optimal viscosity ($\eta_{opt} = 6 \cdot 10^{13} - 10^{19}$ Pa s) and associated maximal heating rate ($H = 10^{-7} - 10^{-6}$ W m^{-3}). Indeed, even if the optimal viscosity may roughly lie around the melting point of the ice, the viscosity relevant to tidal frequencies is not necessarily the same (e.g., smaller) as the convective viscosity. Besides, some anelastic dissipation mechanisms in the ice may be activated at low temperatures (i.e., high viscosity) [e.g., *Castillo-Rogez et al.*, 2011; *McCarthy and Castillo-Rogez*, 2013]. To (roughly) take such uncertainties into account, we explore a wide range of optimal viscosities, keeping in mind that equation (A1) relies on a simple Maxwell viscoelastic rheology.
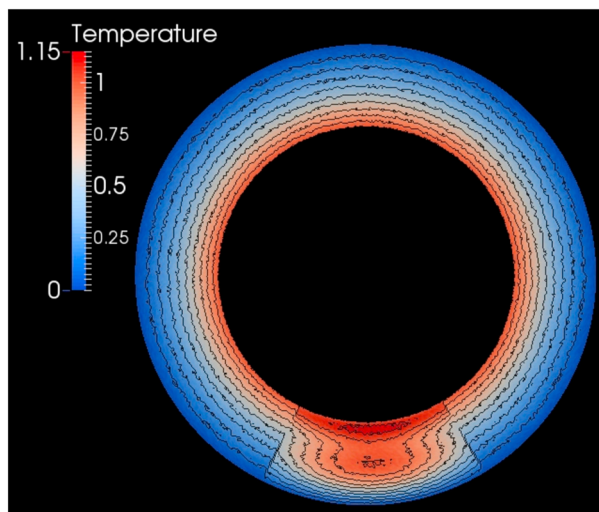
Figure B1. Initial non-dimensional temperature field used for all simulations. Top and bottom temperatures are fixed to 0 and 1 respectively. See text for a detailed description.

Appendix B: Initial Temperature Field

Since we are investigating the stability field of an a priori subcritical plume, it is important to describe the initial temperature field. The initial dimensionless temperature field is defined by

$$\begin{cases} T = \cos^{16}\left(\frac{\pi}{2}\frac{r-r_i}{h}\right) - \sin\left(\pi\frac{r-r_i}{h}\right)\cos^5\theta + N & \text{in SPT,} \\ T = 4.9384\,(h/r) - 1.7778 + N & \text{elsewhere} \end{cases} \tag{B1}$$

with θ as the colatitude, and N stands for a random white noise ranging between -0.025 and 0.025.

Figure B1 shows that the northern hemisphere is first cold (slightly colder than the diffusive temperature profile) and the southern hemisphere exhibits a hot thermal anomaly. This initial temperature distribution ensures the convection to start at least for some time, even if the Rayleigh number may be very low. In case the Rayleigh number is too high to sustain the single-plume state, one or several additional plumes form before the thermal steady-state of the south pole plume is reached. Furthermore, to allow secondary plumes to be generated, some white noise is added everywhere to the initial temperature field.

In the Newtonian cases, the presence of initial noise ensures that the convection is subcritical if it persists without secondary plumes (super-critical convection would start secondary plumes). In non-Newtonian simulations, since convection is always subcritical [*Solomatov*, 2012], the noise may actually start secondary plumes if it is able to generate a stress anomaly sufficiently large to counteract the initially locking effect of the stress-dependent term of the viscosity.

Appendix C: Grain Size, Stresses and Onset of Convection

We observe that the recrystallized grain size is large (at least 1 m). Though it seems surprising, we show in this appendix that this is consistent with previous studies. *Barr and McKinnon* [2007] performed a detailed study of the equilibrium grain size to be expected in the Jovian satellite Europa, for different choices of parameters. We compare here our prediction to this study. The piezometric grain size is directly obtained from the deviatoric stresses. We show here that a larger equilibrium grain size is expected in Enceladus than in Europa using a scaling of the stresses.

The stresses reached in a convecting material depend on the Rayleigh number and on a reference viscosity and strain rate. For a given Rayleigh number, one can compute the stress ratio between different planets or satellites. Equation (9) can be used to define the reference viscosity as a function of the Rayleigh number. The reference strain rate is given by $\dot{\epsilon}_0 = \kappa/h^2$. The stress ratio between Enceladus and Europa can then be computed (again assuming a Rayleigh number):

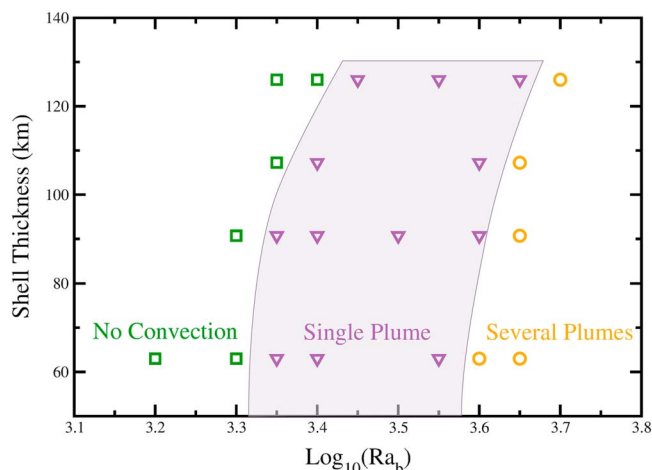$$\frac{\tau_{Eu}}{\tau_{En}} = \frac{\eta_{Eu}\dot{\epsilon}_{Eu}}{\eta_{En}\dot{\epsilon}_{En}}, \tag{C1}$$

Figure D1. Convection regimes map as a function of Rayleigh number and shell thickness (using the activation energy $E = 30$ kJ mol^{-1} and $n' = 3.55$). We use the same color code as in Figure 1.

where "Eu" denotes Europa and "En" stands for Enceladus. If we consider identical physical and rheological properties for Europa and Enceladus, only gravity and shell thickness significantly differs between the two satellites. Using the viscosity defined in equation (9), the stress ratio then becomes

$$\frac{\tau_{Eu}}{\tau_{En}} = \frac{g_{Eu} h_{Eu}}{g_{En} h_{En}}. \tag{C2}$$

For a shell thickness of 90 km and a surface temperature of $\sim$70 K, *Barr and McKinnon* [2007] find a recrystallized grain size of 7 cm, using a calibration consistent with experimental data. The gravity ratio between the two satellites is 0.112/1.3. Using equation (3), we see that this generates then a grain size ratio of $(0.112/1.3)^{-1.25} \simeq 21$, for the same shell thickness (a similar approach is also used by *Barr and Milkovich* [2008]). The piezometric grain size should then be 1.5 m in Enceladus, when ignoring the Rayleigh number effect. Moreover, we argue here that the Rayleigh number could be small in Enceladus to make this subcritical convection behavior possible. This would again decrease the magnitude of the stresses in our model of Enceladus and make the piezometric grain size larger. Using the same approach to compare the grain size ratio between Enceladus and the Earth (using appropriate densities, temperature scales, gravities, and thicknesses), we find that the grain size in the Earth should be about 10^6 times smaller than in Enceladus. The predicted grain size in the Earth, with this very simplified argument should then be around 10 microns, which is an acceptable size.

We do not pretend that this very large grain size should be reached in Enceladus. It has been already shown that the presence of impurities may slow down grain growth, or even limit the maximal grain size. Yet, *Bercovici and Ricard* [2012a, 2012b] show that a nonequilibrium grain size dynamic can generate very nonlinear rheologies, and even localize the deformation. Thus, whatever the state reached by the grain size distribution in a convecting body, the rheology is likely to be non-Newtonian.

If the grain size reaches a large value, the onset of convection may be impossible if the rheology is grain size-dependent [*Barr and Pappalardo*, 2005]. Yet, if the grain size grows to the very large values predicted by equation (3), dislocation creep would dominate and a large grain size would not decrease the viscosity. A detailed study on the onset of convection in a non-Newtonian fluid has been performed by *Barr et al.* [2004]. *Han and Showman* [2011] also investigated the onset of convection with a consistent tidal heating model and a non-Newtonian rheology. The nonequilibrium dynamics of grain size is beyond the scope of the present study. The fact that a non-Newtonian rheology makes the single-plume state more likely would most probably be still valid.

Appendix D: Effect of Ice Shell Thickness

It has been shown that the size of the core, or equivalently a large inner boundary curvature, has a strong effect on the convection degree [*Schubert et al.*, 1990; *Zhong et al.*, 2000; *Grott et al.*, 2007]. In our situation,

we will talk about shell thickness instead of core size because of the potential presence of the basal liquid ocean, of unknown thickness. Thus, knowing the radius of the satellite, a thick shell makes the curvature of the base large. We show here that the shell thickness does not significantly affect the likelihood of the single-plume state. Figure D1 shows that the range of Rayleigh numbers for which the single-plume state is stable is largely unaffected by the shell thickness. Tidal heating is neglected in these additional simulations.

For sake of consistency with our previous computations, we use an initial temperature state in which the anomaly has the same lateral size over mantle thickness ratio as in previous simulations. We investigate mantle thicknesses from 63 to 126 km. For very small shell thicknesses, the shell curvature tends to become negligible. The single-plume state is then stable in the same range of Rayleigh numbers, which explains why the regime boundaries become vertical at the bottom of Figure D1. For ice shells thicker than the one employed in our main model the geometry makes the single plume stable at higher Rayleigh numbers because the average temperature stabilizes at a low value when the inner boundary curvature f increases [*Sotin and Labrosse*, 1999; *Deschamps et al.*, 2010]. The Rayleigh number has then to be slightly increased to make convection possible. However, it can be seen that the single-plume state can be reached in all cases.

References

Alikina, O., and E. Tarunin (2000), Subcritical motions of a fluid with temperature-dependent viscosity, *Fluid Dyn.*, *36*, 574–580.

Ashby, M., and P. Duval (1985), The creep of polycrystalline ice, *Cold Reg. Sci. Technol.*, *11*, 285–300.

Barr, A., and W. B. McKinnon (2007), Convection in ice I shells and mantles with self-consistent grain size, *J. Geophys. Res.*, *112*, E02012, doi:10.1029/2006JE002781.

Barr, A., and S. Milkovich (2008), Ice grain size and the rheology of the martian polar deposits, *Icarus*, *194*, 513–518.

Barr, A., and R. T. Pappalardo (2005), Onset of convection in the icy Galilean satellites: Influence of rheology, *J. Geophys. Res.*, *110*, E12005, doi:10.1029/2004JE002371.

Barr, A., R. Pappalardo, and S. Zhong (2004), Convective instability in ice I with non-Newtonian rheology: Application to the icy Galilean satellites, *J. Geophys. Res.*, *109*, E12008, doi:10.1029/2004JE002296.

Barr, A. C. (2008), Mobile lid convection beneath Enceladus' south polar terrain, *J. Geophys. Res.*, *113*, E07009, doi:10.1029/2008JE003114.

Barr, A. C., and W. B. McKinnon (2007), Convection in Enceladus' ice shell: Conditions for initiation, *Geophys. Res. Lett.*, *34*, L09202, doi:10.1029/2006GL028799.

Bercovici, D., and Y. Ricard (2012a), Mechanisms for the generation of plate tectonics by two-phase grain-damage and pinning, *Phys. Earth Planet. Inter.*, *202-203*, 27–55.

Bercovici, D., and Y. Ricard (2012b), Generation of plate tectonics with two-phase grain-damage and pinning: Source-sink model and toroidal flow, *Earth Planet. Sci. Lett.*, *365*, 275–288.

Besserer, J., G. Tobie, G. Choblet, O. Cadek, and C. Sotin (2008), Liquid Water and Thermal Activity of Enceladus' South Polar Terrain, *AGU Fall Meeting Abstracts*, p. D3.

Besserer, J., F. Nimmo, J. H. Roberts, and R. T. Pappalardo (2013), Convection-driven compaction as a possible origin of Enceladus's long wavelength topography, *J. Geophys. Res. Planets*, *118*, 908–915, doi:10.1002/jgre.20079.

Bland, M. T., K. N. Singer, W. B. McKinnon, and P. M. Schenk (2012), Enceladus' extreme heat flux as revealed by its relaxed craters, *Geophys. Res. Lett.*, *39*, L17204, doi:10.1029/2012GL052736.

Busse, F. (1967), The stability of finite amplitude cellular convection and its relation to an extremum principle, *J. Fluid Mech.*, *30*, 625–649.

Běhounková, M., G. Tobie, G. Choblet, and O. Čadek (2010), Coupling mantle convection and tidal dissipation: Applications to Enceladus and Earth-like planets, *J. Geophys. Res.*, *115*, E09011, doi:10.1029/2009JE003564.

Běhounková, M., G. Tobie, G. Choblet, and O. Čadek (2011), Tidally induced thermal runaways on extrasolar earths: impact on habitability, *Astrophys. J.*, *728*, 89, doi:10.1088/0004-637X/728/2/89.

Běhounková, M., G. Tobie, G. Choblet, and O. Čadek (2012), Tidally-induced melting events as the origin of south-pole activity on Enceladus, *Icarus*, *219*, 655–664, doi:10.1016/j.icarus.2012.03.024.

Běhounková, M., G. Tobie, G. Choblet, and O. Čadek (2013), Impact of tidal heating on the onset of convection in Enceladus's ice shell, *Icarus*, *226*, 898–904, doi:10.1016/j.icarus.2013.06.033.

Castillo-Rogez, J. C., M. Efroimsky, and V. Lainey (2011), The tidal history of Iapetus: Spin dynamics in the light of a refined dissipation model, *J. Geophys. Res.*, *116*, E09008, doi:10.1029/2010JE003664.

Chen, E. M. A., and F. Nimmo (2011), Obliquity tides do not significantly heat Enceladus, *Icarus*, *214*, 779–781, doi:10.1016/j.icarus.2011.06.007.

Christensen, U. (1983), Convection in a variable-viscosity fluid: Newtonian versus power-law rheology, *Earth Planet. Sci. Lett.*, *64*, 153–162.

Christensen, U. (1985), Heat transprot by variable viscosity convection II: Pressure influence, non-Newtonian rheology and decaying heat sources, *Phys. Earth Planet. Inter.*, *37*, 183–205.

Christensen, U. (1989), Mantle rheology, constitution, and convection, in *Mantle Convection, Plate Tectonics and Global Dynamics*, edited by W. R. Peltier, pp. 595–655, Gordon and Breach Sci. Publish., New York.

Coble, R. (1963), A model for boundary diffusion controlled creep in polycrystalline materials, *J. Appl. Phys.*, *34*, 1679–1682.

Collins, G. C., and J. C. Goodman (2007), Enceladus' south polar sea, *Icarus*, *189*, 72–82, doi:10.1016/j.icarus.2007.01.010.

Crow-Willard, E., and R. T. Pappalardo (2011), Global geological mapping of Enceladus. EPSC-DPS Joint Meeting 2011, held 2-7 October 2011 in Nantes, France, p. 635.

De Bresser, J., J. T. Heege, and C. Spiers (2001), Grain size reduction by dynamic recrystallization: Can it result in major rheological weakening? *Int. J. Earth Sci.*, *90*, 28–45.

De La Chapelle, S., O. Castelnau, V. Lipenkov, and P. Duval (1998), Dynamic recrystallization and texture development in ice as revealed by the study of deep ice cores in Antarctica and Greenland, *J. Geophys. Res.*, *103*(B3), 5091–5105.

Deschamps, F., P. Tackley, and T. Nakagawa (2010), Temperature and heat flux scalings for isoviscous thermal convection in spherical geometry, *Geophys. J. Int.*, *182*(1), 137–154, doi:10.1111/j.1365-246X.2010.04637.x.

Durand, G., et al. (2006), Effect of impurities on grain growth in cold ice sheets, *J. Geophys. Res.*, *111*, F01015, doi:10.1029/2005JF000320.

Duval, P. (1981), Creep and fabrics of polycrystalline ice under shear and compression, *J. Glaciol.*, *27*, 129–140.

Duval, P., M. Ashby, and I. Anderman (1983), Rate-controlling processes in the creep of polycrystalline ice, *J. Phys. Chem.*, *87*, 4066–4074.

Foley, B., and T. Becker (2009), Generation of plate-like behavior and mantle heterogeneity form a spherical, viscoplastic convection model, *Geochem. Geophys. Geosyst.*, *10*, Q08001, doi:10.1029/2009GC002378.

Fowler, A. C. (1985), Fast thermoviscous convection, *Stud. Appl. Math.*, *72*, 189–219.

Frost, H., and M. Ashby (1982), *Deformation-Mechanism Maps: The Plasticity and Creep of Metals and Ceramics*, Pergamon Press, Oxford.

Goldsby, D. (2007), Diffusion creep of ice: Constraints from laboratory creep experiments, *38th Lunar and Planetary Science Conference, (Lunar and Planetary Science XXXVIII),* held March 12-16, 2007 in League City, Texas, LPI Contribution No. 1338, p. 2186.

Goldsby, D., and D. Kohlstedt (2001), Superplastic deformation of ice: Experimental observations, *J. Geophys. Res.*, *106*(B6), 11,017–11,030.

Grott, M., F. Sohl, and H. Hussmann (2007), Degree-one convection and the origin of Enceladus' dichotomy, *Icarus*, *191*, 203–210, doi:10.1016/j.icarus.2007.05.001.

Hall, C., and E. Parmentier (2003), Influence of grain size evolution on convective instability, *Geochem. Geophys. Geosyst.*, *4*(3), 1029, doi:10.1029/2002GC000308.

Han, L., and A. Showman (2005), Thermo-compositional convection in Europa's icy shell with salinity, *Geophys. Res. Lett.*, *32*, L20201, doi:10.1029/2005GL023979.

Han, L., and A. Showman (2010), Coupled convection and tidal dissipation in Europa's ice shell, *Icarus*, *207*, 834–844.

Han, L., and A. Showman (2011), Coupled convection and tidal dissipation in Europa's ice shell using non-Newtonian grain-size-sensitive (GSS) creep rheology, *Icarus*, *212*, 262–267.

Han, L., G. Tobie, and A. P. Showman (2012), The impact of a weak south pole on thermal convection in Enceladus' ice shell, *Icarus*, *218*, 320–330, doi:10.1016/j.icarus.2011.12.006.

Hand, K. P., K. K. Khurana, and C. F. Chyba (2011), Joule heating of the south polar terrain on Enceladus, *J. Geophys. Res.*, *116*, E04010, doi:10.1029/2010JE003776.

Harder, H. (2000), Mantle convection and the dynamic geoid of Mars, *Geophys. Res. Lett.*, *27*, 301–304.

Harder, H., and U. Christensen (1996), A one-plume model of Martian mantle convection, *Nature*, *380*, 507–509.

Hemingway, D., F. Nimmo, and L. Iess (2013), Enceladus' internal structure inferred from analysis of Cassini-derived gravity and topography, Abstract P53E–03 presented at 2013 Fall Meeting, AGU, San Francisco, California, 13 Dec.

Hernlund, J. W., and P. J. Tackley (2008), Modeling mantle convection in the spherical annulus, *Phys. Earth Planet. Inter.*, *171*(1-4), 48–54, doi:10.1016/j.pepi.2008.07.037, recent Advances in Computational Geodynamics: Theory, Numerics and Applications.

Herring, C. (1950), Diffusional viscosity of a polycrystalline solid, *J. Appl. Phys.*, *21*, 437–445.

Hirth, G., and D. Kohlstedt (2003), Rheology of the upper mantle and the mantle wedge: A view from the experimentalists, in *Subduction Factor Monograph*, vol. 138, edited by J. Eiler, pp. 83–105, AGU, Washington, D. C.

Howett, C. J. A., J. R. Spencer, J. Pearl, and M. Segura (2011), High heat flow from Enceladus' south polar region measured using 10-600 cm^{-1} Cassini/CIRS data, *J. Geophys. Res.*, *116*, E03003, doi:10.1029/2010JE003718.

Iess, L., M. Parisi, M. Ducci, R. A. Jacobson, J. W. Armstrong, S. W. Asmar, J. I. Lunine, D. J. Stevenson, and P. Tortora (2013), The gravity field of Enceladus from the three Cassini flybys, Abstracts P53B–1859 presented at 2013 Fall Meeting, AGU, San Francisco, Calif.

Jacka, T., and L. Jun (1994), The steady state crystal of deforming ice, *Ann. Glaciol.*, *20*, 13–18.

Jacka, T., and M. Maccagnan (1984), Ice crystallographic and strain rate changes with strain in compression and extension, *Cold Reg. Sci. Technol.*, *8*, 269–286.

Jouzel, J., J. Petit, R. Souchez, N. Barkov, V. Lipenkov, D. Raynaud, M. Stievenard, N. Vassiliev, V. Verbeke, and F. Vimeux (1999), More than 200 meters of lake ice above subglacial lake vostok, antarctica, *Science*, *286*(5447), 2138–2141, doi:10.1126/science.286.5447.2138.

Jung, H., and S. Karato (2001), Water-induced fabric transitions in olivine, *Science*, *293*(5534), 1460–1463.

Jung, H., I. Katayama, Z. Jiang, T. Hiraga, and S. Karato (2006), Effect of water and stress on the lattice-preferred orientation of olivine, *Tectonophysics*, *421*, 1–22.

Karato, S.-i., M. Toriumi, and T. Fujii (1980), Dynamic recrystallization of olivine single crystals during high-temperature creep, *Geophys. Res. Lett.*, *7*, 649–652.

Keller, T., and P. J. Tackley (2009), Towards self-consistent modeling of the Martian dichotomy: The influence of one-ridge convection on crustal thickness distribution, *Icarus*, *202*(2), 429–443, doi:10.1016/j.icarus.2009.03.029.

Kirby, S., W. Durham, M. Beeman, H. Heard, and M. Daley (1987), Inelastic properties of ice Ih at low temperatures and high pressures, *J. Phys.*, *48*, 227–242.

Kohlstedt, D. (2007), Properties of rocks and minerals - constitutive equations, rheological behavior, and viscosity of rocks, in *Treatise on Geophysics*, vol. 2, edited by G. Price, pp. 389–417, Elsevier, Oxford.

Kohlstedt, D. G. D. (1997), Grain boundary sliding in fine-grained ice I, *Scr. Mater.*, *37*, 1399–1406.

Lainey, V., et al. (2012), Strong tidal dissipation in Saturn and constraints on Enceladus' thermal state from astrometry, *Astrophys. J.*, *752*, 14, doi:10.1088/0004-637X/752/1/14.

Mancktelow, N. S. (1987), Quartz textures from the simplon fault zone, southwest Switzerland and North Italy, *Tectonophysics*, *135*(1-3), 133–153.

Matson, D. L., J. C. Castillo-Rogez, A. G. Davies, and T. V. Johnson (2012), Enceladus: A hypothesis for bringing both heat and chemicals to the surface, *Icarus*, *221*, 53–62, doi:10.1016/j.icarus.2012.05.031.

McCarthy, C., and J. Castillo-Rogez (2013), Planetary ices attenuation properties, in *The Science of Solar System Ices, Astrophysics and Space Science Library*, vol. 356, edited by M. Gudipati, and J. Castillo-Rogez, pp. 183–225, Springer, New York.

McKinnon, W. (2006), On convective instability in the ice I shells of outer solar system bodies, with detailed application to callisto, *Icarus*, *183*, 435–450.

McKinnon, W. (2013), The shape of Enceladus as explained by an irregular core: Implications for gravity, libration, and survival of its subsurface ocean, *J. Geophys. Res. Planets*, *118*, 1775–1788, doi:10.1002/jgre.20122.

McNamara, A., and S. Zhong (2005), Degree-one mantle convection: Dependence on internal heating and temperature-dependent rheology, *Geophys. Res. Lett.*, *32*, L01301, doi:10.1029/2004GL021082.

Meyer, J., and J. Wisdom (2007), Tidal heating in Enceladus, *Icarus*, *188*, 535–539, doi:10.1016/j.icarus.2007.03.001.

Meyer, J., and J. Wisdom (2008), Episodic volcanism on Enceladus: Application of the Ojakangas Stevenson model, *Icarus*, *198*, 178–180, doi:10.1016/j.icarus.2008.06.012.

Mitri, G., and A. P. Showman (2008), Thermal convection in ice-I shells of Titan and Enceladus, *Icarus*, *193*, 387–396, doi:10.1016/j.icarus.2007.07.016.

Moresi, L., and V. Solomatov (1998), Mantle convection with a brittle lithosphere: Thoughts on the global tectonic style of the Earth and Venus, *Geophys. J.*, *133*, 669–682.

Morris, S., and D. Canright (1984), A boundary-layer analysis of Benard convection in a fluid of strongly temperature-dependent viscosity, *Phys. Earth Planet. Inter.*, *36*, 355–373.

Nabarro, F. (1948), Deformation of crystals by the motion of single ions, in *Report on a Conference on the Strength of Solids*, pp. 75–90, Physical society, London.

Nakajima, M., and A. Ingersoll (2012), Can the Enceladus plume account for 16 GW? A boiling liquid model, *AGU Fall Meeting Abstracts*, pp. P33A–1919.

Nimmo, F., and R. T. Pappalardo (2006), Diapir-induced reorientation of Saturn's moon Enceladus, *Nature*, *441*, 614–616, doi:10.1038/nature04821.

Nimmo, F., J. R. Spencer, R. T. Pappalardo, and M. E. Mullen (2007), Shear heating as the origin of the plumes and heat flux on Enceladus, *Nature*, *447*, 289–291, doi:10.1038/nature05783.

Nimmo, F., B. G. Bills, and P. C. Thomas (2011), Geophysical implications of the long-wavelength topography of the Saturnian satellites, *J. Geophys. Res.*, *116*, E11001, doi:10.1029/2011JE003835.

Ojakangas, G. W., and D. J. Stevenson (1986), Episodic volcanism of tidally heated satellites with application to Io, *Icarus*, *66*, 341–358, doi:10.1016/0019-1035(86)90163-6.

Olgin, J. G., B. R. Smith-Konter, and R. T. Pappalardo (2011), Limits of Enceladus's ice shell thickness from tidally driven tiger stripe shear failure, *Geophys. Res. Lett.*, *38*, L02201, doi:10.1029/2010GL044950.

O'Neill, C., and F. Nimmo (2010), The role of episodic overturn in generating the surface geology and heat flow on Enceladus, *Nat. Geosci.*, *3*, 88–91, doi:10.1038/ngeo731.

Parmentier, E., and J. Morgan III (1982), Thermal convection in non-Newtonian fluids: Volumetric heating and boundary layer scaling, *J. Geophys. Res.*, *87*, 7757–7762.

Parmentier, E., D. Turcotte, and K. Torrance (1976), Studies of finite amplitude non-Newtonian thermal convection with application to convection in the Earth's mantle, *J. Geophys. Res.*, *81*, 1839–1846.

Patankar, S. (1980), *Numerical Heat Transfer and Fluid Flow*, McGraw-Hill, New York.

Patthoff, D. A., and S. A. Kattenhorn (2011), A fracture history on Enceladus provides evidence for a global ocean, *Geophys. Res. Lett.*, *38*, L18201, doi:10.1029/2011GL048387.

Poirier, J. (1985), *Creep of Crystals: High-Temperature Deformation Processes in Metal, Ceramics and Minerals*, Cambridge Univ. Press, Cambridge.

Porco, C. C., et al. (2006), Cassini Observes the Active South Pole of Enceladus, *Science*, *311*, 1393–1401, doi:10.1126/science.1123013.

Rainey, E., and D. Stevenson (2005), Grain size-dependent viscosity and oceans in icy satellites, *36th Annual Lunar and Planetary Science Conference,* in League City, Texas, abstract no.2100 March 14–18, 2005.

Reese, C. C., V. S. Solomatov, and L.-N. Moresi (1998), Heat transport efficiency for stagnant lid convection with dislocation viscosity: Application to Mars and Venus, *J. Geophys. Res.*, *103*, 13,643–13,657.

Ricard, Y., and D. Bercovici (2009), A continuum theory of grain size evolution and damage, *J. Geophys. Res.*, *114*, B01204, doi:10.1029/2007JB005491.

Roberts, J. (2013), Tidal dissipation in a frozen Enceladus, *44th Lunar and Planetary Science Conference,* held March 18-22, 2013 in The Woodlands, Texas, LPI Contribution No. 1719, p.1317.

Roberts, J., and S. Zhong (2006), Degree-1 convection in the Martian mantle and the origin of the hemispheric dichotomy, *J. Geophys. Res.*, *111*, E06013, doi:10.1029/2005JE002668.

Roberts, J., and S. Zhong (2007), The cause for the north-south orientation of the crustal dichotomy and the equatorial location of Tharsis on Mars, *Icarus*, *190*, 24–31.

Roberts, J. H., and F. Nimmo (2008a), Tidal heating and the long-term stability of a subsurface ocean on Enceladus, *Icarus*, *194*, 675–689, doi:10.1016/j.icarus.2007.11.010.

Roberts, J. H., and F. Nimmo (2008b), Near-surface heating on Enceladus and the south polar thermal anomaly, *Geophys. Res. Lett.*, *35*, L09201, doi:10.1029/2008GL033725.

Ross, M. N., and G. Schubert (1989), Viscoelastic models of tidal heating in Encedalus, *Icarus*, *78*, 90–101, doi:10.1016/0019-1035(89)90071-7.

Rozel, A. (2012), Impact of grain size on the convection of terrestrial planets, *Geochem. Geophys. Geosyst.*, *13*, Q10020, doi:10.1029/2012GC004282.

Rozel, A., Y. Ricard, and D. Bercovici (2011), A thermodynamically self-consistent damage equation for grain size evolution during dynamic recrystallization, *Geophys. J. Int.*, *184*(2), 719–728, doi:10.1111/j.1365-246X.2010.04875.x.

Schenk, P. M., and W. B. McKinnon (2009), One-hundred-km-scale basins on Enceladus: Evidence for an active ice shell, *Geophys. Res. Lett.*, *36*, L16202, doi:10.1029/2009GL039916.

Schmidt, K. G. K., and D. Dahl-Jensen (2003), An ice crystal model for Jupiter's moon Europa, *Ann. Glaciol.*, *37*(1), 129–133.

Schubert, G., D. Bercovici, and G. A. Glatzmaier (1990), Mantle dynamics in Mars and Venus - Influence Of an immobile lithosphere on 3-dimensional mantle convection, *J. Geophys. Res.*, *95*(B9), 14,105–14,129.

Schubert, G., D. Turcotte, and P. Olson (2001), *Mantle Convection in the Earth and Planets*, Cambridge Univ. Press, Cambridge.

Schubert, G., J. D. Anderson, B. J. Travis, and J. Palguta (2007), Enceladus: Present internal structure and differentiation by early and long-term radiogenic heating, *Icarus*, *188*, 345–355, doi:10.1016/j.icarus.2006.12.012.

Segel, L., and J. Stuart (1962), On the question of the preferred mode in cellular thermal convection, *J. Fluid Mech.*, *13*, 289–306.

Shimizu, I. (1998b), Stress and temperature dependence of recrystallized grain size: A subgrain misorientation model, *Geophys. Res. Lett.*, *25*, 4237–4240.

Shimizu, I. (2008), Theories and applicability of grain size piezometers: The role of dynamic recrystallization mechanisms, *J. Struct. Geol.*, *30*, 899–917.

Shoji, D., H. Hussmann, K. Kurita, and F. Sohl (2013), Ice rheology and tidal heating of Enceladus, *Icarus*, *226*, 10–19.

Showman, A., L. Han, and W. Hubbard (2013), The effect of an assymmetric core on convection in Enceladus's ice shell: Implications for south polar tectonics and heat flux, *Geophys. Res. Lett.*, *40*, 5610–5614, doi:10.1002/2013GL057149.

Smith, C. (1948), Grains, phases, interfaces: An interpretation of microstructures, *Trans. Met. Soc. AIME*, *175*, 15–51.

Smolarkiewicz, P. (1984), A fully multidimensional positive definite advection transport algorithm with small implicit diffusion, *J. Comput. Phys.*, *54*, 325–362.

Solomatov, V. (2001), Grain size-dependent viscosity convection and the thermal evolution of the Earth, *Earth Planet. Sci. Lett.*, *191*, 203–212.

Solomatov, V. (2012), Localized subcritical convective cells in temperature-dependent viscosity fluids, *Phys. Earth Planet. Inter.*, *200-201*, 63–71.

Solomatov, V., and C. Reese (2008), Grain size variations in the earth's mantle and the evolution of primordial chemical heterogeneities, *J. Geophys. Res.*, *113*, B07408, doi:10.1029/2007JB005319.

Solomatov, V. S. (1995), Scaling of temperature- and stress-dependent viscosity convection, *Phys. Fluids*, *7*, 266–274.

Sotin, C., and S. Labrosse (1999), Three-dimensional thermal convection in an iso-viscous, infinite prandtl number fluid heated from within and from below: Applications to the transfer of heat through planetary mantles, *Phys. Earth Planet. Inter.*, *112*, 171–190.

Spencer, J., and F. Nimmo (2013), Enceladus: An active ice world in the Saturn system, *Annu. Rev. Earth Planet. Sci.*, *41*, 693–717.

Spencer, J., J. Pearl, M. Segura, F. Flasar, A. Mamoutkine, P. Romani, B. Buratti, A. Hendrix, L. Spilker, and R. Lopes (2006), Cassini encounters Enceladus: Background and the discovery of a south polar hot spot, *Science*, *311*, 1401–1405, doi:10.1126/science.1121661.

Spencer, J., C. Howett, A. Verbiscer, T. Hurford, M. Segura, and D. Spencer (2013), Enceladus heat flow from high spatial resolution thermal emission observations, *EPSC Abstracts 8* (EPSC2013-840-1).

Spitale, J. N., and C. C. Porco (2007), Association of the jets of Enceladus with the warmest regions on its south-polar fractures, *Nature*, *449*, 695–697, doi:10.1038/nature06217.

Squyres, S. W., R. T. Reynolds, and P. M. Cassen (1983), The evolution of Enceladus, *Icarus*, *53*, 319–331, doi:10.1016/0019-1035(83)90152-5.

Stegman, D. R., J. Freeman, and D. A. May (2009), Origin of ice diapirism, true polar wander, subsurface ocean, and tiger stripes of Enceladus driven by compositional convection, *Icarus*, *202*, 669–680, doi:10.1016/j.icarus.2009.03.017.

Stein, C., J. Schmalzl, and U. Hansen (2004), The effect of rheological parameters on plate behaviour in a self-consistent model of mantle convection, *Phys. Earth Planet. Inter.*, *142*, 225–255.

Stevenson, D. (1980), Lunar symmetry and paleomagnetism, *Nature*, *287*, 520–521.

Stevenson, D. J., L. Iess, M. Parisi, M. Ducci, and S. W. Asmar (2013), The interpretation of Enceladus gravity, *AGU Fall Meeting Abstracts*, pp. P53E–01.

Tackley, P. (1993), Effects of strongly temperature-dependent viscosity on time-dependent, 3-dimensional models of mantle convection, *Geophys. Res. Lett.*, *20*(20), 2187–2190.

Tackley, P. J. (1996), On the ability of phase transitions and viscosity layering to induce long-wavelength heterogeneity in the mantle, *Geophys. Res. Lett.*, *23*, 1985–1988.

Tackley, P. J. (2000), Self consistent generation of tectonic plates in time-dependent, three dimensional mantle convection simulations, part 1: Pseudoplastic yielding, *Geochem. Geophys. Geosyst.*, *1*, 1021, doi:10.1029/2000GC000036.

Tackley, P. J. (2008), Modelling compressible mantle convection with large viscosity contrasts in a three-dimensional spherical shell using the Yin-Yang grid, *Phys. Earth Planet. Inter.*, *171*(1-4), 7–18.

Tobie, G., G. Choblet, and C. Sotin (2003), Tidally heated convection: Constraints on Europa's ice shell thickness, *J. Geophys. Res.*, *108*(E11), 5124, doi:10.1029/2003JE002099.

Tobie, G., A. Mocquet, and C. Sotin (2005), Tidal dissipation within large icy satellites: Applications to Europa and Titan, *Icarus*, *177*, 534–549, doi:10.1016/j.icarus.2005.04.006.

Tobie, G., O. Čadek, and C. Sotin (2008), Solid tidal friction above a liquid water reservoir as the origin of the south pole hotspot on Enceladus, *Icarus*, *196*, 642–652, doi:10.1016/j.icarus.2008.03.008.

Tyler, R. (2011), Tidal dynamical considerations constrain the state of an ocean on Enceladus, *Icarus*, *211*, 770–779, doi:10.1016/j.icarus.2010.10.007.

Tyler, R. H. (2009), Ocean tides heat Enceladus, *Geophys. Res. Lett.*, *36*, L15205, doi:10.1029/2009GL038300.

Van der Wal, D., P. Chopra, M. R. Drury, and J. D. Fitzgerald (1993), Relationships between dynamically recrystallized grain size and deformation conditions in experimentally deformed olivine rocks, *Geophys. Res. Lett.*, *20*, 1479–1482.

van Heck, H. J., and P. J. Tackley (2008), Planforms of self-consistently generated plates in 3D spherical geometry, *Geophys. Res. Lett.*, *35*, L19312, doi:10.1029/2008GL035190.

Vissers, R. L. M., M. R. Drury, E. H. H. Strating, C. J. Spiers, and D. van der Wal (1995), Mantle shear zones and their effect on lithosphere strength during continental breakup, *Tectonophysics*, *249*(3-4), 155–171, doi:10.1016/0040-1951(95)00033-J.

Šrámek, O., and S. Zhong (2012), Martian crustal dichotomy and tharsis formation by partial melting coupled to early plume migration, *J. Geophys. Res.*, *117*, E01005, doi:10.1029/2011JE003867.

Walker, C. C., J. N. Bassis, and M. W. Liemohn (2012), On the application of simple rift basin models to the south polar region of Enceladus, *J. Geophys. Res.*, *117*, E07003, doi:10.1029/2012JE004084.

Weinstein, S. A. (1995), The effects of a deep mantle endothermic phase change on the structure of thermal convection in silicate planets, *J. Geophys. Res.*, *100*(E6), 11,719–11,728.

Wise, D., M. Golombek, and G. E. McGill (1979), Tectonic evolution of mars, *J. Geophys. Res.*, *84*, 7934–7939.

Yoshida, M. (2008), Mantle convection with longest-wavelength thermal heterogeneity in a 3-D spherical model: Degree one or two?, *Geophys. Res. Lett.*, *35*, L23302, doi:10.1029/2008GL036059.

Yoshida, M., and A. Kageyama (2006), Low-degree mantle convection with strongly temperature- and depth-dependent viscosity in a three-dimensional spherical shell, *J. Geophys. Res.*, *111*, B03412, doi:10.1029/2005JB003905.

Yoshida, M., and M. Santosh (2011), Supercontinents, mantle dynamics and plate tectonics: A perspective based on conceptual vs. numerical models, *Earth Sci. Rev.*, *105*(1-2), 1–24.

Zhang, K., and F. Nimmo (2009), Recent orbital evolution and the internal structures of Enceladus and Dione, *Icarus*, *204*, 597–609, doi:10.1016/j.icarus.2009.07.007.

Zhang, S., S.-I. Karato, J. FitzGerald, U. Faul, and Y. Zhou (2000), Simple shear deformation of olivine aggregates, *Tectonophysics*, *316*, 133–152.

Zhong, S., and M. Zuber (2001), Degree-1 mantle convection and the crustal dichotomy on Mars, *Earth Planet. Sci. Lett.*, *190*, 75–84.

Zhong, S., E. Parmentier, and M. T. Zuber (2000), A dynamic origin for global asymmetry of lunar mare basalts, *Earth Planet. Sci. Lett.*, *177*, 131–141.